
Masters Theses

Student Theses and Dissertations

Summer 2020

Modal analysis as non-destructive testing technique for additively manufactured 304L stainless steel parts

Tristan N. Cullom

Follow this and additional works at: https://scholarsmine.mst.edu/masters_theses



Part of the [Mechanical Engineering Commons](#)

Department:

Recommended Citation

Cullom, Tristan N., "Modal analysis as non-destructive testing technique for additively manufactured 304L stainless steel parts" (2020). *Masters Theses*. 8073.

https://scholarsmine.mst.edu/masters_theses/8073

This thesis is brought to you by Scholars' Mine, a service of the Missouri S&T Library and Learning Resources. This work is protected by U. S. Copyright Law. Unauthorized use including reproduction for redistribution requires the permission of the copyright holder. For more information, please contact scholarsmine@mst.edu.

MODAL ANALYSIS AS NON-DESTRUCTIVE TESTING TECHNIQUE FOR
ADDITIVELY MANUFACTURED 304L STAINLESS STEEL PARTS

by

TRISTAN NICHOLAS CULLOM

A THESIS

Presented to the Graduate Faculty of the
MISSOURI UNIVERSITY OF SCIENCE AND TECHNOLOGY

In Partial Fulfillment of the Requirements for the Degree
MASTER OF SCIENCE IN MECHANICAL ENGINEERING

2020

Approved by:

Robert Landers, Advisor

Edward Kinzel

Douglas Bristow

© 2020

Tristan Nicholas Cullom

All Rights Reserved

PUBLICATION THESIS OPTION

This thesis consists of the following two articles, formatted in the style used by the Missouri University of Science and Technology:

Paper I: Pages 8-28 are intended for submission to Additive Manufacturing Journal.

Paper II: Pages 29-55 are intended for submission to Scientific Reports Journal.

ABSTRACT

Non-Destructive Testing (NDT) methods for Additively Manufactured (AM) parts is an ongoing field of research in the additive community due to its ability to determine if a part can be deemed viable for field usage. This study presents modal analysis as a NDT method for AM parts. For production builds that have multiple copies of the same part, a correcting technique can be used such that the frequencies of the parts under test can be reliably compared against each other, which saves both time and money compared to other traditional NDT methods. This study was able to develop a novel method for quantifying the processing force that develops over the melt pool during the Selective Laser Melting (SLM) process. The processing force was found to be dependent on the laser power, Pulse Repetition Frequency (PRF), and scanning speed, which are the primary processing parameters of the SLM process. Modal analysis is shown to be a promising NDT method and future work will be done to look at an algorithmic framework for analyzing an arbitrary part with modal analysis.

ACKNOWLEDGMENTS

I am extremely grateful to my advisors, Dr. Robert Landers, Dr. Edward Kinzel, and Dr. Douglas Bristow for their support and guidance throughout my graduate study. Their cumulative knowledge about selective laser melting is amazing and it gave me the opportunity to grow as both a person and an engineer. Their patience and willingness to let me explore engineering topics that were not initially thought of was very beneficial for me.

I am very appreciative to have worked with my fellow lab mates. This work would not have been possible without them and my time in graduate school allowed me to cultivate very strong friendships – Cody Lough, and Jason Johnson.

I am particularly grateful for both the faculty at Michigan Technological University as well as the employees at Honeywell for their ongoing support and collaboration for the project.

I would like to thank my all my friends and family, my parents Jason and Steffany, for their constant love and support and over my graduate years.

Finally, I would like to thank and acknowledge the financials supports of this work. This work was funded by Honeywell Federal Manufacturing & Technologies under Contract No. DE-NA0002839 with the U.S. Department of Energy. The United States Government retains and the publisher, by accepting the article for publication, acknowledges that the United States Government retains a nonexclusive, paid up, irrevocable, world-wide license to publish or reproduce the published form of this manuscript, or allow others to do so, for the United States Government purposes.

TABLE OF CONTENTS

	Page
PUBLICATION THESIS OPTION	iii
ABSTRACT	iv
ACKNOWLEDGMENTS	v
LIST OF ILLUSTRATIONS	viii
LIST OF TABLES	xi
NOMENCLATURE.....	xii
 SECTION	
1. INTRODUCTION AND LITERATURE REVIEW	1
1.1. INTRODUCTION INTO ADDITIVE MANUFACTURING.....	1
1.2. INTRODUCTION TO MODAL ANALYSIS	5
 PAPER	
I. EFFECTS OF IDENTICAL PARTS ON A COMMON BUILD PLATE ON THE MODAL ANALYSIS OF SLM CREATED METAL.....	8
ABSTRACT	8
1. INTRODUCTION	8
2. COUPLING WITH PLATE.....	10
3. COUPLING WITH OTHER PARTS	18
4. MITIGATION TECHNIQUES FOR COUPLING EFFECT	22
4.1. SPARSE BUILDS.....	22
4.2. DENSE BUILDS	23
5. SUMMARY	27

REFERENCES	27
II. FREQUENCY DOMAIN MEASUREMENTS OF MELT POOL RECOIL FORCE USING MODAL ANALYSIS.....	29
ABSTRACT.....	29
1. INTRODUCTION	29
2. EXPERIMENTAL SET-UP	34
3. EXPERIMENTAL RESULTS.....	39
3.1. SINGLE LINE SCAN PATH WITHOUT POWDER.....	39
3.2. RASTER SCAN PATH WITH LAYER OF POWDER.....	43
3.3. MEASUREMENTS OF MELT POOL AFTER SOLIDIFICATION	48
4. METHODS.....	50
4.1. MATERIALS	50
4.2. RECOIL FORCE MAGNITUDE CORRECTION.....	50
4.3. UNCERTAINTY CALCULATION	51
5. SUMMARY	52
REFERENCES	53
SECTION	
2. CONCLUSIONS.....	56
REFERENCES	57
VITA.....	59

LIST OF ILLUSTRATIONS

SECTION	Page
Figure 1.1: Renishaw AM250 chamber design.....	2
Figure 1.2: Exposure scan path.	3
Figure 1.3: Scan pattern after layer rotation.	4
Figure 1.4: (a) ANSYS bracket model with arrow showing direction of forcing and (b) Resulting FRF in same direction as force.....	6
 PAPER I	
Figure 1: Coupling example for parts on common build plate.....	9
Figure 2: Damped 2DOF analytical model to approximate single cantilever on build plate.	10
Figure 3: Frequency response from ANSYS simulation.	11
Figure 4: Analytical and simulation FRF comparison.....	12
Figure 5: Frequency and modal mass relationship for (a) first mode and (b) second mode of 2DOF model.....	13
Figure 6: Spatial sweep notation.	14
Figure 7: Uncertainty in (a) frequency and (b) modal mass for swept part across build plate cross section.....	15
Figure 8: Uncertainty in (a) yield strength and (b) density for swept part across build plate.	16
Figure 9: (a) First build plate mode contour (b) Second build plate mode contour.	16
Figure 10: First modal frequency of part as function of modal mass of build plate.	17
Figure 11: Multi-tuned mass spring damper system to approximate behavior for multiple parts on a build plate.....	18

Figure 12: (a) Single in middle (b) Three in horizontal (c) Three in diagonal (d) Five in X layout (e) Five in plus formation (f) 9 in 3×3 formation (g) 25 in 5×5 formation.	20
Figure 13: Frequency response of middle cantilever for configurations (a) through (g)..	21
Figure 14: Synchronized mode for configuration (g).....	22
Figure 15: Eigenfrequencies of (a) first cantilever mode (b) second cantilever mode (c) first build plate mode (d) second build plate mode (e) third cantilever mode and (f) third build plate mode of single cantilever-build plate structure for changes in the modal mass of build plate with horizontal reference lines for fixed-free and free-free boundary condition for cantilever and build plate modes, respectively.....	24
Figure 16: Frequency response of middle cantilever in configuration (g) for density changes of surrounding cantilevers.	25
Figure 17: Mode shape with only middle cantilever moving with masses of other cantilevers shifted up.....	26
Figure 18: Modal mass of (a) middle and (b) synchronized modes for percent changes in mass for rest of structure other than device under test with reference line in (a) corresponding to modal mass of single cantilever on build plate.....	26
 PAPER II 	
Figure 1: Illustrations of (a) laser excitation of tuning fork with accelerometer (Accel) mounted on tuning fork prong, (b) laser interaction with powder on top of tuning fork during laser excitation, and (c) FRFs of tuning forks with varying prong lengths.....	35
Figure 2: (a) Tuning fork build with arrow indicating tuning forks from Table 1 and (b) FRF of tuning fork #16.	38
Figure 3: (a) Normalized photodiode waveform with inset showing raster scan and (b) FFT of photodiode waveform data at $\tau_{\text{Pulse}} = 100 \mu\text{s}$ with and without cornering.	39
Figure 4: (a) Measured FRFs of tuning fork #16, (b) Measured acceleration spectrum with inset showing single line scanning strategy schematic, and (c) Calculated forcing spectrum with SNR spectrum (gray line).....	42
Figure 5: Recoil force versus laser power for tuning forks #15, #16, #17, and #20.	42

Figure 6: (a) Recoil force as function of laser power and scanning speed for constant PRF and powder layer thickness and (b) Recoil force as function of ratio of power to scanning speed.	44
Figure 7: (a) Recoil force as function of laser power and PRF for constant scanning speed and powder layer thickness and (b) Recoil force as function of ratio of power to the square root of PRF.	45
Figure 8: Recoil force as function of $P \cdot DC / V_{Scan}$	46
Figure 9: Recoil force magnitude for having powder spread on surface and having no powder on surface for various laser powers, scanning speeds, and PRFs.	47
Figure 10: (a) Melt pool depth as function of recoil force with and without powder, (b) Melt pool aspect ratio as function of recoil force with horizontal lines indicating dominant heat transfer modes, (c) Melt pool depth for experiments with powder versus melt pool depth for experiments without powder, and (d) Sample micrographs as function of laser power and scanning speed for raster scan paths with and without powder.....	49
Figure 11: Percentage of energy located in fundamental frequency relative to normalized input for photodiode pulse data pure pulse train and raster scan data.....	51

LIST OF TABLES

PAPER II	Page
Table 1: List of tuning forks used in experiments with their resonant frequencies.	36
Table 2: Chemical composition of 304L stainless steel powder.	50

NOMENCLATURE

Symbol	Description
P	Laser Power
v	Scanning Speed
s	Laser Spot Size
ρ	Density
E	Young's Modulus
E	Young's Modulus
h	Hatch Spacing
FFT	Fast Fourier Transform
FRF	Frequency Response Function
M^M	Modal Mass
φ	Modal Vector
Δf	Frequency Resolution of Time Domain FFT
Δt	Time Sample Interval
$F_{Nyquist}$	Nyquist Frequency of Discretely Sampled Data
F_{Sample}	Sampling Frequency of Discretely Sampled Data
N	Number of Time Points Over which Fourier Transform is Performed
F_{Sample}	Time Sample Interval

1. INTRODUCTION AND LITERATURE REVIEW

1.1. INTRODUCTION INTO ADDITIVE MANUFACTURING

Selective Laser Melting (SLM) is an Additive Manufacturing (AM) process that uses a laser in an inert atmosphere to selectively melt layers of metal powder into a solid part; this process is achieved by building a part layer by layer starting from the bottom to the top. AM is a relatively new form of manufacturing that began during the mid-1980's. The first AM technologies that were developed were Stereolithography, dealing with polymers, and Selective Laser Sintering (SLS), dealing with metals, which were developed in 1987 and 1992, respectively. [1]

One of the main distinctions between AM technologies and traditional manufacturing technologies is that ability to produce parts that would otherwise be considered impossible to produce. In the medical industry, custom implants can be made that are fitted for a patient that reduce the wait time for traditional methods from months to mere hours [2]. In addition to implants, AM has also developed bioprinting which involves printing living tissue that can be used for skin, bone, organs, and other vital tissues [3]. In the automation industry, AM allows prototypes to be made to speed up the time-to-market speed to help expedite concepts [4]. The capabilities of AM can only be fully explored by expanding the usages of AM as well as the techniques themselves that are used to produce parts.

The Renishaw AM250 Laser Melting Machine is a commercially available SLM machine that was used in the research shown in this paper. A diagram of the build chamber can be seen in Figure 1.1.

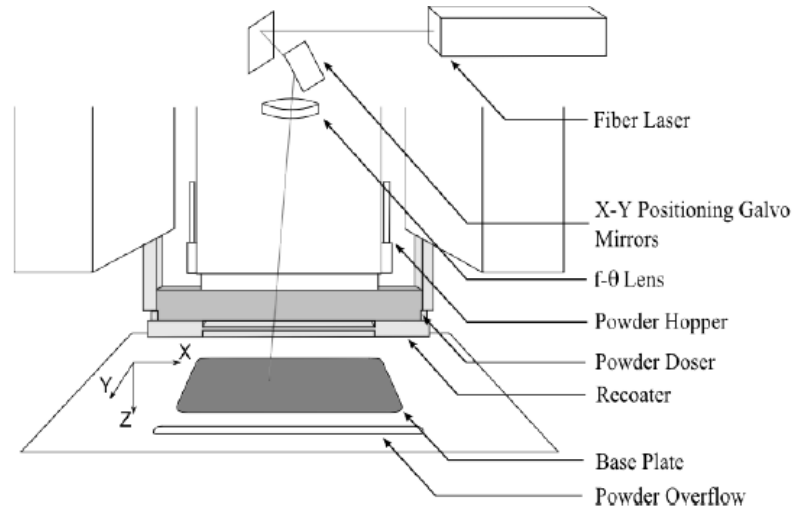


Figure 1.1: Renishaw AM250 chamber design. [5]

For this machine, the process of printing a part starts with a base plate bolted to an elevator that moves in the Z-axis. A recoater compresses springs on a powder doser that allow powders to be deposited in front of the recoater. The elevator is moved down by a layer thickness and is then brought forward in the positive Y-axis; this allows a single layer of powder to be spread along the base plate and any excessive powder is dispensed into the powder overflow. A laser beam is then positioned on the base plate using an f- θ lens where it is then focused and melts the powders on the base plate to form each layer of the part that is being printed. The laser scan path follows a pattern for each layer of the part, with illustrations shown in Figure 1.2 and Figure 1.3.

The Renishaw AM250 uses a scan pattern where a single point along a scan path is exposed with the laser, then the laser turns off, moves to the next point and then exposes the new point. The scan path shown in Figure 1.2 is the base scanning strategy for each

layer; after the laser finishes scanning over the part geometry, the recoater re-doses a layer of powder and the process is repeated.

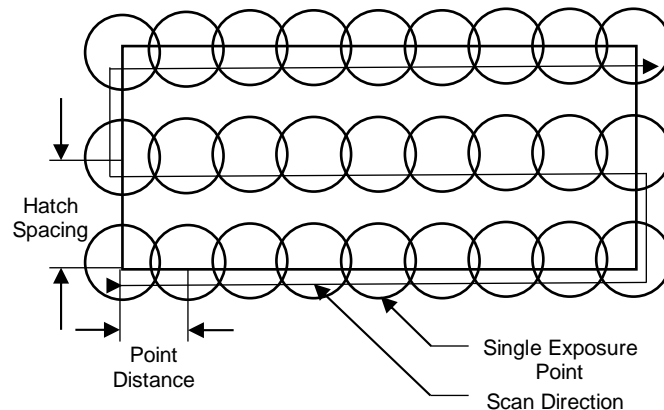


Figure 1.2: Exposure scan path.

For each layer, the layer is rotated by a fixed rotation angle, shown in Figure 1.3 in order to prevent points from being exposed in multiple layers. Scanning strategies such as the ones shown with the AM250 allow for fine detail parts to be printed that would not be able to be achieved with continuous scanning laser systems.

Even with the novel scanning strategy that is presented above, issues can arise during the scanning process that can affect the quality of the part. Porosity, incomplete fusion holes, cracks, and residual stresses are some of the most common types of defects that can occur during the SLM process [6]. Studies have looked at processing parameters of SLM systems and their effects on the defects [7]–[9] in the effort to determine ways to minimize these defects.

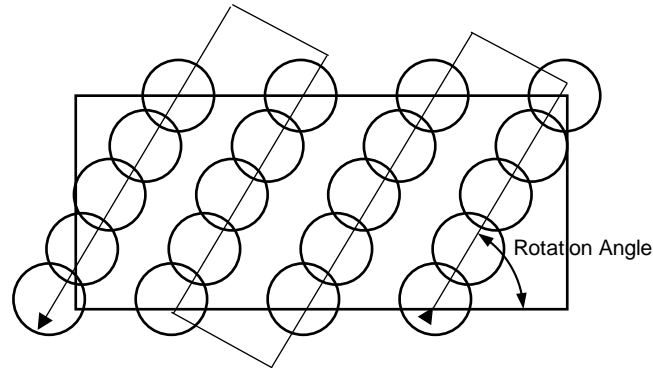


Figure 1.3: Scan pattern after layer rotation.

Another field of research deals with ways of validating parts to identify whether a part has formed a defect that would deem it unusable in the field. Such methods can be separated into two groups: destructive and non-destructive. Tensile testing is a type of destructive testing that can produce engineering properties such as young's modulus, yield strength, and ultimate strength; these properties can be greatly useful distinguishing defective parts from good parts. Non-Destructive Testing (NDT) is the other group of testing that deals with monitoring the parts as they print or analyzing the parts after they are printed to validate whether they can be deemed useful. Thermography and acoustic emissions are two of the most common NDT methods that are used in SLM [10]. Thermography can be used to monitor the melt pool as the part is printing but is faced with calibration issues given the broad temperature range of the melt pool. Acoustic emissions can be used to base defects on changes in the signal but often requires extensive filtering to isolate a signal that would be deterministic of a defect. In the effort to bypass calibration and filtering, another NDT method that shows promise for validating parts is called modal analysis, which is the subject of research in this paper.

1.2. INTRODUCTION TO MODAL ANALYSIS

Modal analysis is the study of a part's dynamic response in the frequency domain. For a given part, there exists an infinite number of frequencies that the part resonates at, which are the points at which the dynamic response is amplified. Each frequency of a part follows a relationship between the young's modulus, density, and a mode-specific coefficient that dictates that magnitude of the frequency,

$$f \propto \alpha^2 \sqrt{\frac{E}{\rho}} \quad (1)$$

where α^2 is the mode specific coefficient, E is the young's modulus, and ρ is the density of the part. With Equation (1), if a part were to have a defect, the stiffness and mass of the part would change, resulting in a different frequency from a part that did not have a defect. Modal analysis can be seen used back as early as the 1770s for defect detection through wheel-tappers, or people that would walk along the length of the train and check wheels for signs of damages in the form of the tone they produced when hit [11]. In AM, the same principle can be extended towards AM parts by looking at the natural frequencies of the parts to determine if there is porosity in the part that could lead to failure when used in the field. For modal analysis, the way that the frequency content of a part is studied is in the form of a Frequency Response Function (FRF). An FRF is a linear transfer function that is defined as the Fourier Transform of a time domain input. To calculate the FRF, a structure is excited with a given force and the motion is measured with a transducer.

To illustrate a FRF, an ANSYS simulation was ran in which a topology optimized bracket was excited with a horizontal force and the FRF in the same direction of the force

was calculated. A figure of the topology bracket with an arrow illustrating the direction of the force and the resulting FRF is shown in Figure 1.4. The FRF that is calculated from a structure is ultimately dependent on the direction that the structure is excited. When excited with a horizontal force shown in Figure 1.4a, the only frequencies that are excited are the frequencies in which the mode of the bracket is moving in the horizontal direction, which are shown as the insets of Figure 1.4b.

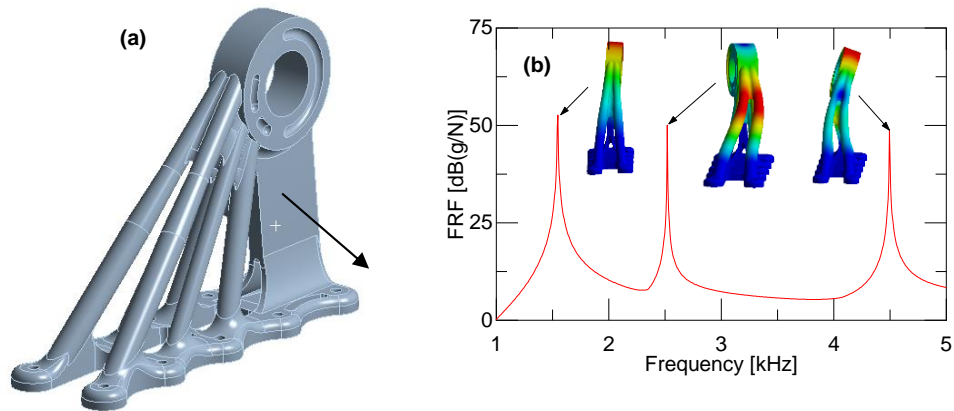


Figure 1.4: (a) ANSYS bracket model with arrow showing direction of forcing and (b) Resulting FRF in same direction as force.

The FRF can be an identifying function of a defect if the frequencies of the same mode are compared against multiple parts. In a study with 304L stainless steel, correlations were able to be found between engineering properties, porosity, and processing parameters for parts that were used with a Renishaw AM250 [12]. These correlations were novel but were only for parts that were unique on the build plate (i.e. there were no duplicates of the same part that were tested). Using the FRF the test dense builds of the same part, which is

typical for a production setting, there are concerns with determining the frequency of the mode of interest because of a phenomenon known as coupling. The coupling phenomenon can yield a false-negative response that would result in a nominal part to be deemed part due to either its location on the build plate or the number of common parts on the plate.

PAPER

I. EFFECTS OF IDENTICAL PARTS ON A COMMON BUILD PLATE ON THE MODAL ANALYSIS OF SLM CREATED METAL

ABSTRACT

Additive Manufacturing (AM) is a growing industry due to its ability to produce complex parts that would otherwise be impossible to make with traditional machining methods. Due to the growing nature of AM, Structural Health Monitoring (SHM) has become a necessity for validation of parts. Modal analysis has been Non-Destructive Evaluation (NDE) method for validating parts but not without its own concerns. A part's frequency changes depending on its location on the build plate that its fixtured to as well as the number of parts on the plate itself; these shifts in frequencies are attributed to the modal mass of the structure. This paper investigates the uncertainty in these frequency changes and the corresponding solutions that can be used to reduce the uncertainty in the validation process.

1. INTRODUCTION

When more than one part is present on a build plate, experimental practice uses a magnitude criterion to dictate the frequency at which that part resonates at. Implementing this validation technique poses concerns however when a single part or multiple parts are placed on the build plate. Variations in the resonate frequency of a part change as a function

of both the location as well as the number of parts on the plate. When the mode shape of the structure is analyzed for multiple parts there is coupling between parts: more than one part move during a mode. Figure 1 showcases these concerns in the form of four configurations.

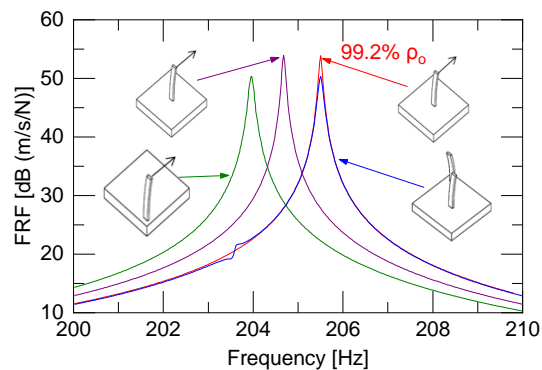


Figure 1: Coupling example for parts on common build plate.

The purple line will be considered as the reference for the other three configurations. If a single part were to be placed simply on the corner instead of the middle, it resonates at a lower frequency than the middle cantilever. Conversely, if the middle cantilever were to possess a defect, which was facilitated as a change in its density, it would resonate at a higher frequency. Similarly, if another cantilever were to be placed on the build plate, the peak response of the signature resonates at the same frequency as the defective part in the middle, even though both cantilevers are nominal. The two peaks for in ascending order are the two cantilevers moving out of phase and in phase, respectively. The changes in frequency for the structure can be decomposed into two physical

interactions: coupling between the part and plate as well as coupling between multiple parts on the plate. These interactions can be quantified as changes to the modal mass of the cantilever modes of the structure. For a continuous system, the modal mass is a representation of the motion of the body in all directions [1]. Structures such as footbridges have had their modal mass approximated to help predict resonant modes that may be excited through human-induced excitation [2]. Other studies have utilized modal mass approximation for the purpose of developing Passive Tuned Mass Dampers (PTMD) to reducing the response of train excitation on bridges [3].

2. COUPLING WITH PLATE

For a single part on a build plate, a mass spring damper system was used to approximate the behavior for the two-part structure which can be seen in Figure 2.

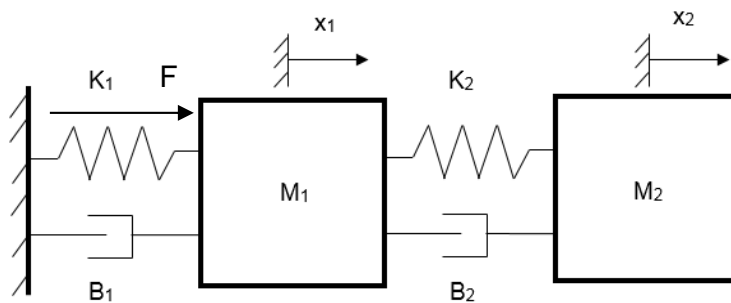


Figure 2: Damped 2DOF analytical model to approximate single cantilever on build plate.

The masses M_1 and M_2 are the representative modal masses of the build plate and cantilever, respectively. Damping was ignored for the purpose of calculating the eigenfrequencies due to the damping coefficient being sufficiently low such that the damped natural frequency is approximately equal to the natural. The eigenvalues were calculated accordingly and can be seen in Equation 2.

$$\omega_{1,2} = \sqrt{\frac{(K_1 + K_2)M_2 + K_2M_1 \pm \sqrt{M_2^2(K_1^2 + 2K_1K_2 + K_2^2) - M_1M_2(2K_1K_2 - 2K_2^2) + K_2^2M_1^2}}{2M_1M_2}} \quad (2)$$

The validity of the model was measured through a comparison with an ANSYS simulation. A single cantilever was modeled in the middle of the build plate with properties set to be 304L stainless steel while the build plate was set to be 1010 structural steel and driven with a corresponding frequency response seen in Figure 3.

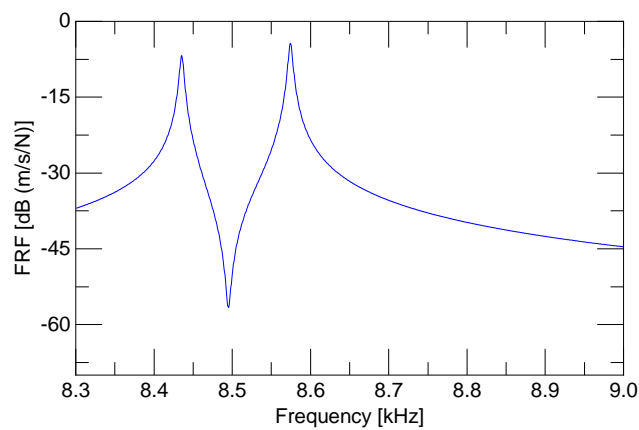


Figure 3: Frequency response from ANSYS simulation.

The transfer function relating the velocity of the cantilever to the imposed force on the build plate was used to fit the model to the driven data, which can be seen in Figure 4.

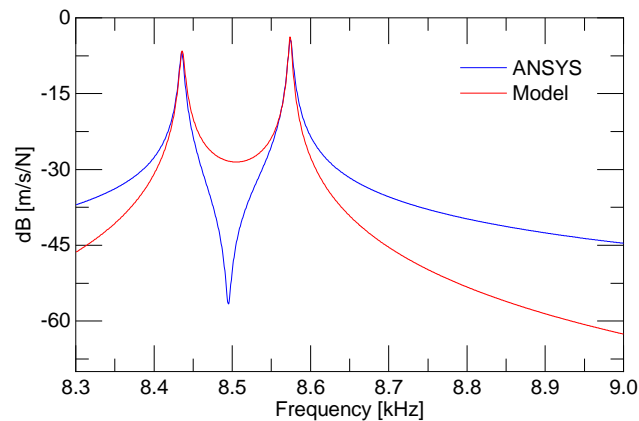


Figure 4: Analytical and simulation FRF comparison.

The model was able to accurately model the frequencies of the structure as well as the magnitude of the response. As the frequency increases towards that of infinity, the model's response can be seen to diverge towards zero. The ANSYS response does not show this behavior since there are an infinite number of modes influencing the response. With this model, predictions can be made from looking at the sensitivity of the modes of the structure given changes to modal parameters; the parameters in question are the masses of both the cantilever as well as the build plate. The first behavior that can be seen is when the modal mass of the build plate, M_1 , was increased such that it was several orders of magnitude higher than that of M_2 . Figure 5 shows two modes of the discrete model to

changes in the modal mass of M_1 . As the mass of the build plate increases, the first modal frequency, seen in (a), diverges towards that of zero: insinuating that as the mass of the plate approaches that of infinity, it would essentially be a fixed boundary condition. The opposite happens for the second mode of the structure: as the modal mass increases, the frequency of the second mode converges towards that of the frequency of M_2 that would occur if M_2 were isolated.

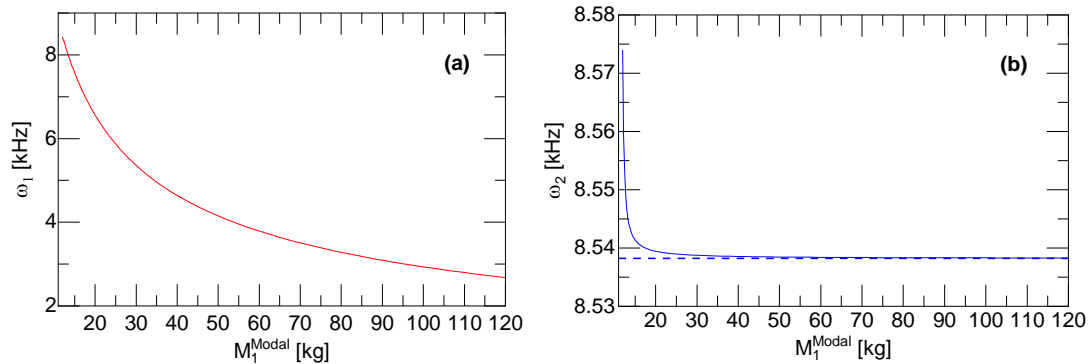


Figure 5: Frequency and modal mass relationship for (a) first mode and (b) second mode of 2DOF model.

Two ANSYS simulations were conducted in which a part was swept across the cross-section of the build plate and comparing the frequency and modal mass of the swept part to a part in the middle as well as having a stationary part and varying the modal mass of the build plate. The purpose of both simulations was to investigate the sensitivity of resonant frequencies to shifts in modal mass of the structure. For the first simulation, Figure 6 shows a representative figure on how the part was swept across the cross-section of the build plate. With each position on the build plate, the first modal frequency was recorded

and a representative contour plot was made in which a difference was plotted which was the difference between each position's frequency and the frequency of the middle as well as the change in modal mass, which can be seen in Figure 7. The change in modal mass for the structure is the reasoning as to why the frequency of the part varies with location.

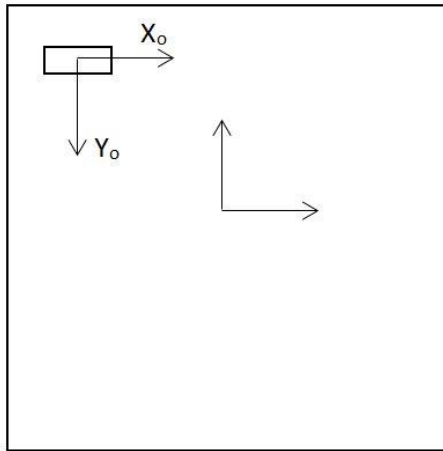


Figure 6: Spatial sweep notation.

With the changes in both frequency and modal mass, there is an uncertainty with distinguishing between parts as a function of these properties. This uncertainty can be extended towards material properties, which studies have already found relationships between the two; B. West et al. found relationships between frequency, density, and yield strength for changes in laser power and hatch spacing [4].

The reasoning behind the relationship had to deal with porosity, which varied depending on hatch spacing and power. Using the fitted equations which were found for parts that resonated in the same frequency range as the part in Figure 7, contour plots

showing the uncertainty about yield strength and density can be made, which can be seen in Figure 8.

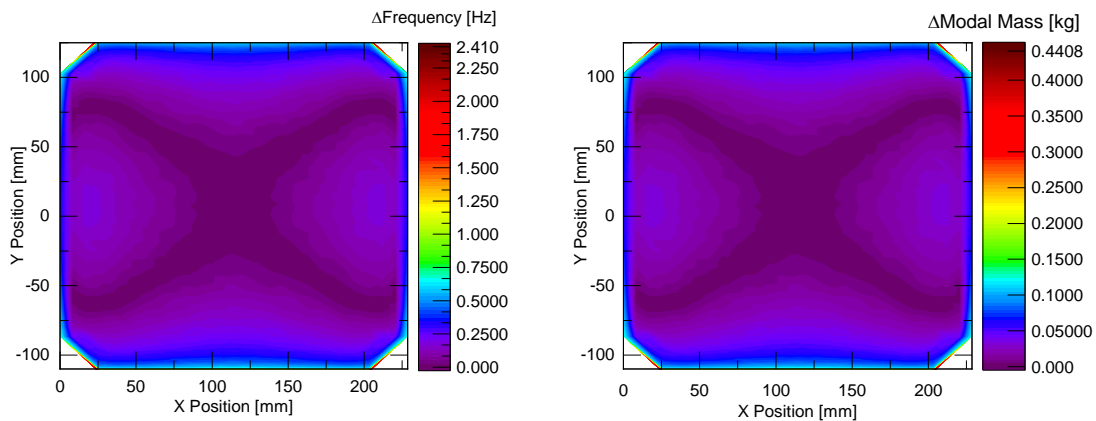


Figure 7: Uncertainty in (a) frequency and (b) modal mass for swept part across build plate cross section.

Since the modal mass is proportional to the mode shape vector, the modes of the build plate that couple to the cantilever can be seen to explain this behavior. Since ANSYS's solution involves an infinite number of modes for the build plate-cantilever structure, it is very difficult to explain the change in frequency to a sole build plate mode. This can be illustrated in Figure 8, which displays the deformation contours of the first two modes of the build plate. Referring to Figure 7, the contour of the swept part looks like that of the second build plate mode even though on a frequency basis alone, a discrete system would predict maximum coupling with the first mode.

This alludes to that fact that for a continuous system, the coupling that exists is also dependent on the difference of mode shape vectors for the part as well as the build plate,

resulting in the similarity between the second mode and the part as opposed to the first mode.

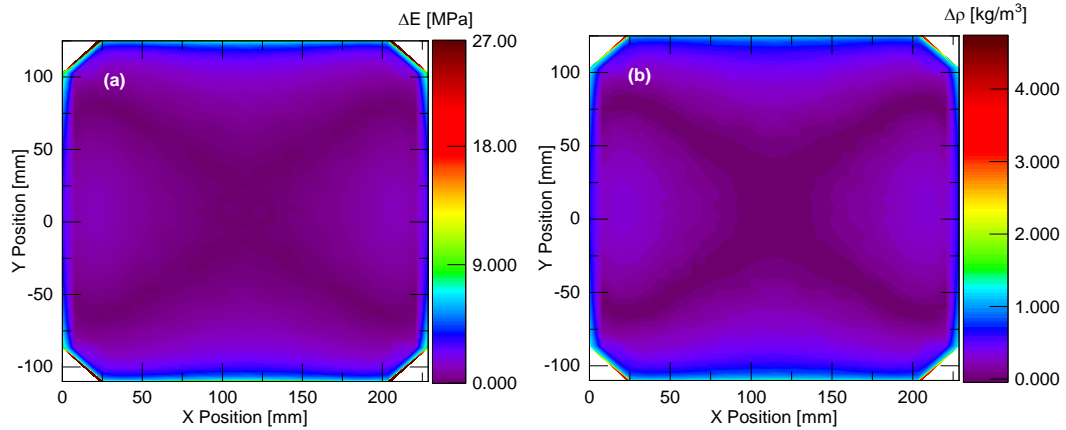


Figure 8: Uncertainty in (a) yield strength and (b) density for swept part across build plate.

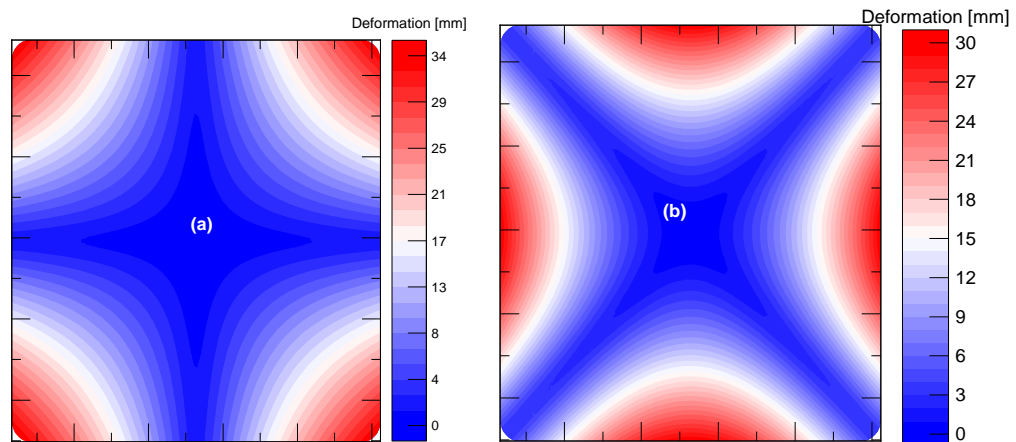


Figure 9: (a) First build plate mode contour (b) Second build plate mode contour.

For the second simulation, the same part as the first was placed in the middle of the build plate. The density of the build plate was increased from nominal 1010 structural steel to 10 times nominal and the first mode of the part was recorded and plotted as a function of the modal mass of the build plate, which can be seen in Figure 10. Like the behavior seen in Figure 5 with the discrete model, the frequency of the part converges towards that of a fixed-free frequency when the ratio of mass between the part and the rest of the structure is sufficiently low. This sensitivity to changes in frequency for part under test for both location and difference in mass between itself and the rest of the structure creates concerns for methodology as to how the part can be properly validated.

Validating a single part on the build plate raises concerns regarding resonant frequencies since the frequency of the part changes as a function of its location on the build plate as well as differences between mass and frequency of the part and build plate.

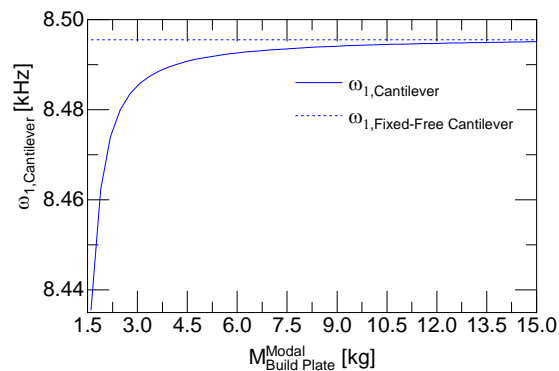


Figure 10: First modal frequency of part as function of modal mass of build plate.

It can be concluded that in order to address the coupling concern between a single part, modifications must be made between the part and the build plate in order to minimize if not suppress coupling.

3. COUPLING WITH OTHER PARTS

For one than one part on a build plate, an additional tuned mass was added to the model discussed in the previous section and can be seen in Figure 11. As the number of parts increases on the build plate, additional masses can be added and be denoted as four through N. The purpose of this model is to show the relationship between the resonate frequencies of the tuned masses, in this case M_2 and M_3 as a function of the build plate mass, M_1 .

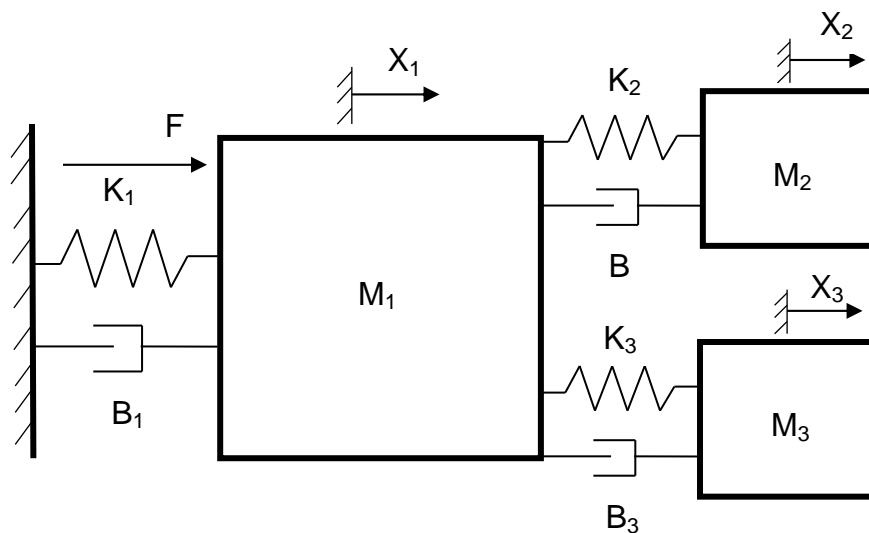


Figure 11: Multi-tuned mass spring damper system to approximate behavior for multiple parts on a build plate.

The characteristic equation for the model in Figure 11 can be seen below.

$$\begin{aligned} & -M_1M_2M_3\omega^6 + (M_2M_3(K_1 + K_2 + K_3) + M_1M_2K_3 + M_1M_3K_2)\omega^4 \\ & - (K_2K_3(M_1 + M_2 + M_3) + M_2K_1K_3 + M_3K_1K_2)\omega^2 + K_1K_2K_3 = 0 \end{aligned} \quad (3)$$

As the equation stands, the only way to solve for the eigenfrequencies would have to be done numerically. However, if an assumption is made such that M_1 is several orders of magnitude higher than the attached masses, Equation 3 simplifies to Equation 4.

$$-M_1M_2M_3\omega^6 + M_1(K_2 + K_3)\omega^4 - M_1K_2K_3\omega^2 + K_1K_2K_3 = 0 \quad (4)$$

If M_1 is several orders of magnitude higher than the stiffnesses allows the equation to again be simplified to Equation 5.

$$-M_1M_2M_3\omega^6 + M_1(M_3K_2 + M_2K_3)\omega^4 - M_1K_2K_3\omega^2 = 0 \quad (5)$$

This equation predicts two non-zero frequencies and one zero frequency. By using the quadratic formula, the two non-zero eigenfrequencies can be written in terms of the parameters and is as follows,

$$\omega_{2,3} = \sqrt{\frac{-(M_3K_2 + M_2K_3) \pm (M_3K_2 - M_2K_3)}{-2M_2M_3}} \quad (6)$$

With these eigenfrequencies, the intrinsic behavior between the build plate and cantilevers is such that that when the build plate is sufficiently large, the uncertainty seen in material properties and frequency becomes zero. When the build plate is not infinitely large however, builds with more than one part, coupling exists if the frequencies of the parts under test are close to each other [5]. Simulations were run in ANSYS in which the

quantity of parts was varied from 1 to 25, with Figure 12 showing each configuration that will be referenced in this section. The parts were evenly spaced in the X and Y directions denoted in Figure 6 with the frequency response of the middle-most cantilever recorded for each configuration. The frequency response of the middle-most cantilever was recorded and plotted as a function of configuration in Figure 13.

As the number of cantilevers increases, the dominant response of the FRF continues to shift towards the right, displaying a divergent behavior. This can be explained in a synchronous mode which can be seen in Figure 14 for configuration (g).

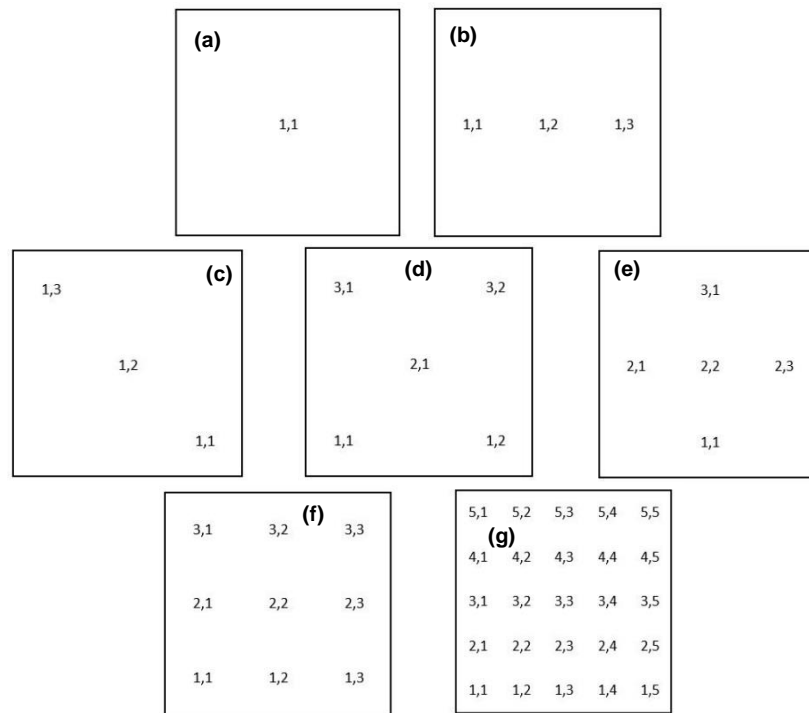


Figure 12: (a) Single in middle (b) Three in horizontal (c) Three in diagonal (d) Five in X layout (e) Five in plus formation (f) 9 in 3×3 formation (g) 25 in 5×5 formation.

This synchronized mode can be explained through energy being shared between the cantilevers given a common fixturing point. Studies have already shown that for parts such as cantilevers, even with their resonant frequencies differing, will converge towards a common frequency in the form of a synchronized mode.

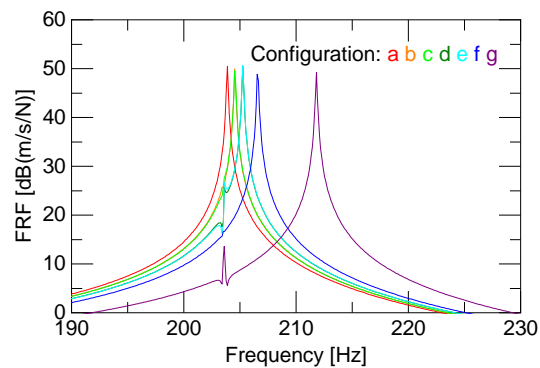


Figure 13: Frequency response of middle cantilever for configurations (a) through (g).

For large builds that consist of multiple parts of the same geometry and properties, the ability to discern between parts using the magnitude validation technique is impossible if the build plate is not fixed. The reasoning behind this is since when parts are coupled through a common medium that is not entirely rigid; the parts are able to sync together in a synchronized mode. Due to this synchronized coupling, the modal mass of that mode dominates the response and dwarfs modes in which less than the maximum number of parts are moving in tandem.

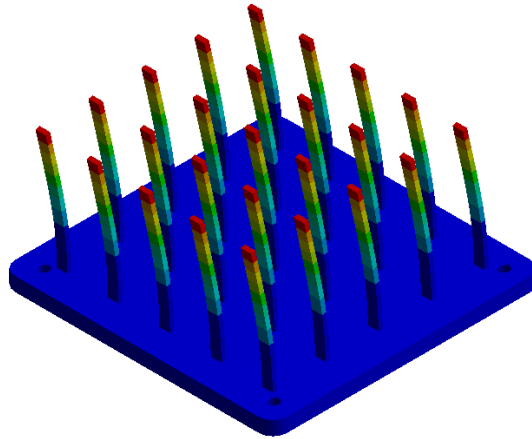


Figure 14: Synchronized mode for configuration (g).

4. MITIGATION TECHNIQUES FOR COUPLING EFFECT

Builds that allow parts to be positioned on points of interest about the build plate modes will be referred to as sparse builds and builds with numerous parts that cannot allow this will be referred to as dense builds. With the coupling effects seen in the previous two sections, techniques may be employed such that the effect is either minimized or removed outright with modifications to either part location or mass of the structure relative to the Device Under Test (DUT), depending on the type of build in question.

4.1. SPARSE BUILDS

For sparse builds, modifications may be made to the mass of the structure relative to the DUT as well as the position of the part itself. The first technique can be seen through an ANSYS simulation. A single cantilever was placed on the corner which has seen to have the largest difference in frequency from that of the middle. The mass to stiffness ratio was

increased of the build plate such that the frequency of the plate's modes did not change but the structural mass did. The first three modes of the part as well as the first three modes of the build plate were recorded and can be seen in Figure 15.

For each graph, a solid line representing the frequency of each isolated part: fixed-free cantilever and free-free for the build plate was plotted against the eigenfrequency data for each of the first six modes. As the modal mass of the build plate increased, the respective eigenfrequencies for both the cantilever and build plate converged towards the isolated cases. This result implies that if the mass of the structure relative to the DUT is sufficiently high, the frequency of the DUT will become the same frequency as if the part were by itself and not fixtured to the build plate.

4.2. DENSE BUILDS

For dense builds, since parts cannot be placed in optimal positions, changes to the relative structural mass can be facilitated in order to remove the coupling effect as well as allow proper validation of the DUT. An ANSYS simulation was conducted with configuration (g) in Section 3 in which the densities of every part aside from the middle were increased to approximate an effective point mass. The densities varied from 110% to 150% the nominal density and the frequency response of the middle cantilever was recorded for each density and plotted in addition to the nominal configuration, which can be seen in Figure 16.

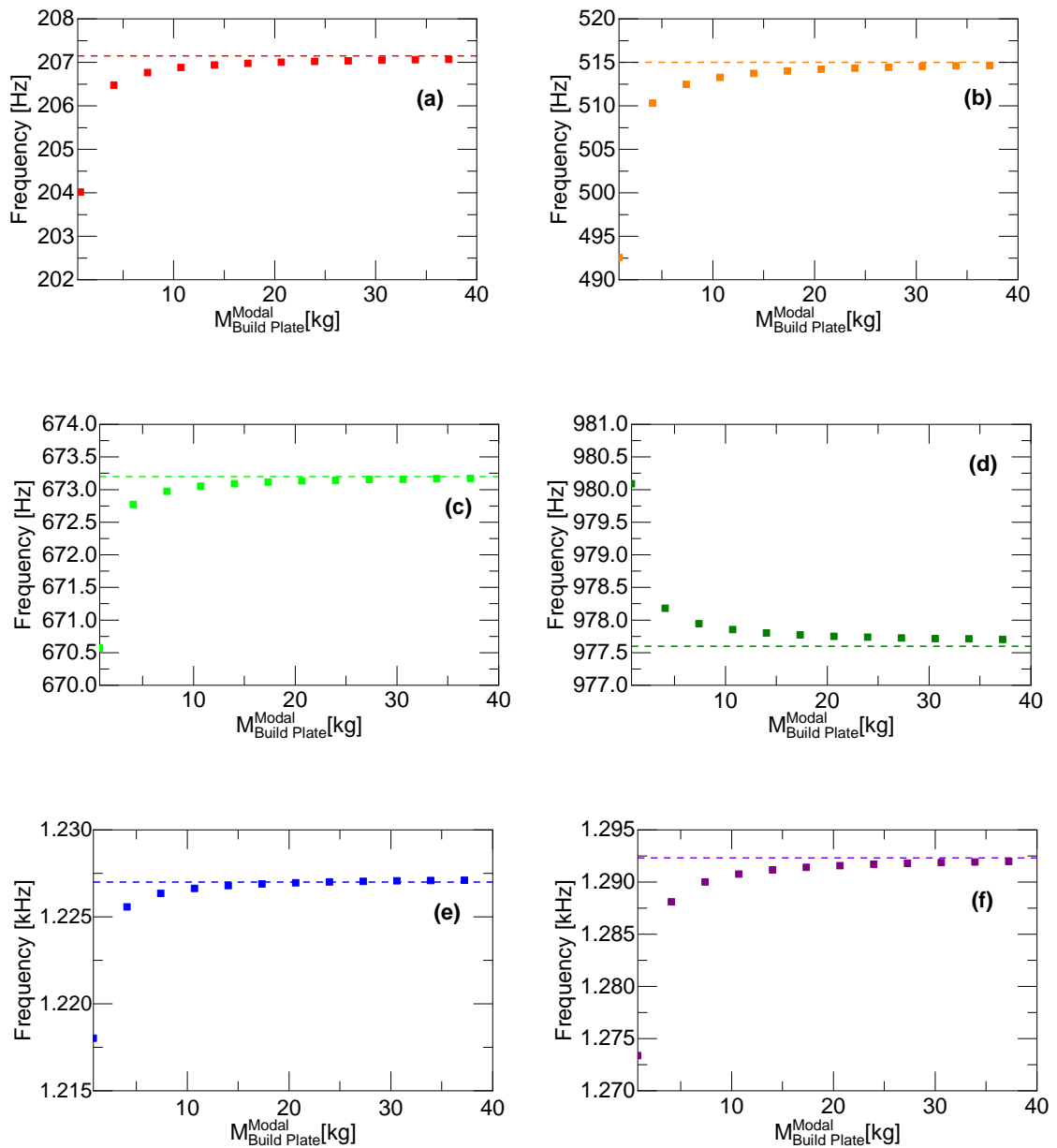


Figure 15: Eigenfrequencies of (a) first cantilever mode (b) second cantilever mode (c) first build plate mode (d) second build plate mode (e) third cantilever mode and (f) third build plate mode of single cantilever-build plate structure for changes in the modal mass of build plate with horizontal reference lines for fixed-free and free-free boundary condition for cantilever and build plate modes, respectively.

Validation was an issue for the nominal configuration since the dominant peak was the synchronized mode with all the cantilevers moving. As the density of the surrounding parts increased however, the dominant peak converged towards a constant value of 207.48 Hz, with Figure 17 showing the mode shape of the structure, which the fixed-free frequency of the same cantilever geometry, which can be seen in Figure 15a.

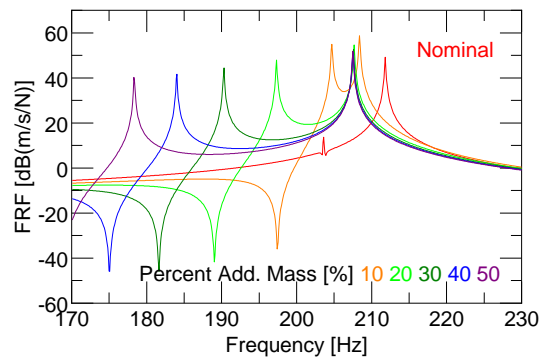


Figure 16: Frequency response of middle cantilever in configuration (g) for density changes of surrounding cantilevers.

In addition to this, the response of the synchronized mode, which is the first peak of each response aside from the nominal curve, continues to decrease with increasing density. This can be explained through the change in modal mass for the single cantilever mode, seen in Figure 17, as well as the synchronized mode, seen in Figure 14, for each configuration, which can be seen in Figure 18.

In Figure 18, the modal mass of the single cantilever decreases for an increase of mass for the surrounding parts. The reasoning behind this is that with the frequency of the

parts shifting further away from the middle, their influence in the mode shape of the isolated part begins to diminish. Conversely, the modal mass of the synchronized mode increases which is expected considering the mass of the rest of the cantilevers increases.

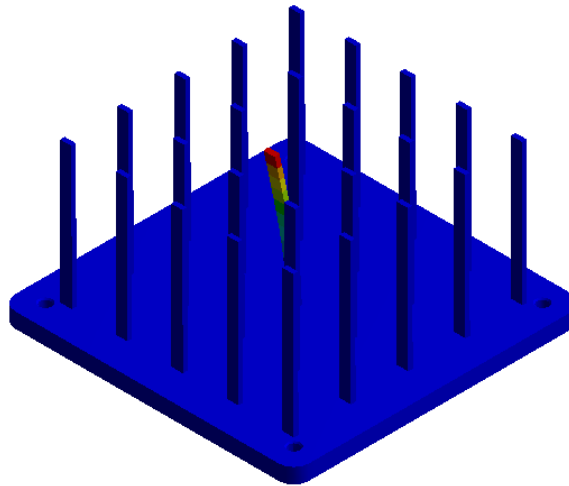


Figure 17: Mode shape with only middle cantilever moving with masses of other cantilevers shifted up.

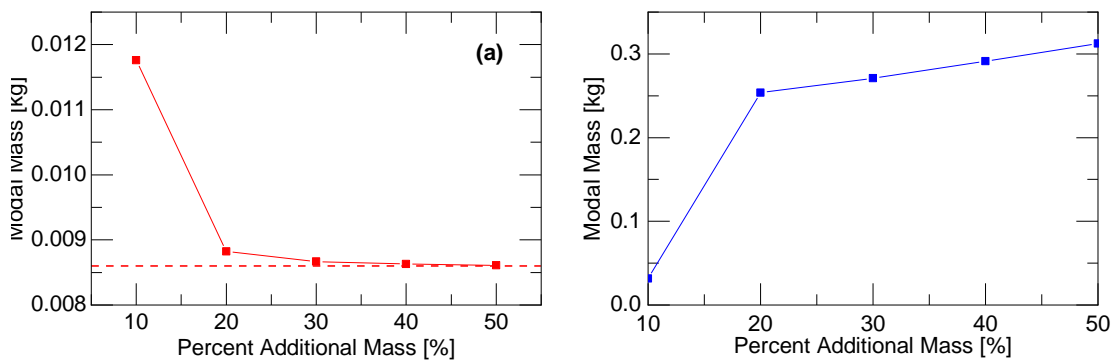


Figure 18: Modal mass of (a) middle and (b) synchronized modes for percent changes in mass for rest of structure other than device under test with reference line in (a) corresponding to modal mass of single cantilever on build plate.

The ability to remove coupling for both sparse and dense builds can be facilitated through a change in modal mass of the rest of the structure relative to the DUT. This can be achieved through either adding point mass to the surrounding parts for dense builds, or simply increasing the overall mass of the build plate that the part is fixtured to. The change in build plate mass can be facilitated through either bolting it to a heavier plate or increasing the thickness of the plate.

5. SUMMARY

Part validation is increasing with the continued growth and popularity of additive manufacturing. In order to validate parts printed using SLM, modal analysis is a tool that is practical in terms of both time and finances. For proper validation however, a concern in the form of changes in resonant frequencies for part(s) fixtured to the plate due to either the location of the part(s) or the number of parts on the plate. Mitigation techniques may be used for both sparse and dense builds in the form of shifting the modal mass of the structure relative to the DUT; positioning the part on nodal lines is another technique that enables proper validation of a part as well as have the frequency of the part approach or converge towards a constant frequency. From this correcting technique, modal analysis appears to be a promising method for validating AM parts.

REFERENCES

- [1] M. H. Richardson, "Modal mass, stiffness and damping," *Measurement*, no. 6, pp. 1–6, 2000.

- [2] J. M. W. Brownjohn and A. Pavic, “Experimental methods for estimating modal mass in footbridges using human-induced dynamic excitation,” *Eng. Struct.*, vol. 29, no. 11, pp. 2833–2843, 2007, doi: 10.1016/j.engstruct.2007.01.025.
- [3] J. F. Wang, C. C. Lin, and B. L. Chen, “Vibration suppression for high-speed railway bridges using tuned mass dampers,” *Int. J. Solids Struct.*, vol. 40, no. 2, pp. 465–491, 2003, doi: 10.1016/S0020-7683(02)00589-9.
- [4] B. M. West *et al.*, “Modal analysis of metal additive manufactured parts,” *Manuf. Lett.*, vol. 13, pp. 30–33, 2017, doi: 10.1016/j.mfglet.2017.06.001.
- [5] M. Spornraft, “Smasis2015-8928 Synchronization of Cantilevers Arranged in Line of a,” pp. 1–7, 2015.

II. FREQUENCY DOMAIN MEASUREMENTS OF MELT POOL RECOIL FORCE USING MODAL ANALYSIS.

ABSTRACT

The recoil pressure is a critical factor affecting the melt pool dynamics during the Selective Laser Melting (SLM) process. Proper recoil pressure depresses the melt pool and improves layer-to-layer fusion. If the recoil pressure is too low, the layers will not fuse, while excessive recoil pressure leads to a keyhole mode, which results in gas porosity. Direct recoil pressure measurements are challenging because it is localized over an area proportionate to the laser spot size producing a force in the mN range. This paper reports a vibration-based approach to quantify the recoil force exerted on a part in a commercial SLM machine. The measured recoil force is consistent with estimates from high speed synchrotron imaging of entrained particles, and the results show that the recoil force scales with laser power and is inversely proportional to the laser Pulse Repetition Frequency (PRF). These results facilitate further studies of melt pool dynamics and have the potential to aid process development for new materials or in-situ monitoring/diagnostics.

1. INTRODUCTION

Selective Laser Melting (SLM) is a powder bed metal additive manufacturing process capable of fabricating functional parts with complex geometries. In this process a build plate is lowered by a fixed distance (i.e., the layer thickness) and a layer of powder is spread across the build plate. The powder is irradiated by a laser beam at specific

locations to fabricate that layer. After the laser finishes scanning the layer, the build plate is lowered, new powder is spread, and the laser again irradiates locations where the part needs to be built on that layer. These steps are repeated until the complete part is printed. When the laser irradiates the powder, a molten pool of metal (i.e., a melt pool) is formed. The final state of the part at the location the laser is irradiating is dictated by the complex dynamics (e.g., heat transfer, material motion) occurring within the melt pool from the moment it forms until the moment it solidifies. Cumulatively, these states determine part quality.

The melt pool dynamics are driven by several forces. Recoil, Marangoni, capillary, and buoyancy are the four main forces that act on the melt pool. Recoil force occurs when the temperature of the surface of the melt pool exceeds the vaporization temperature, causing a recoil pressure on the evaporating surface [1]. The depth of the melt pool, amount of thermal transport, and degree of which material is fused together is driven by the recoil force. Marangoni force occurs due to the large temperature and surface tension gradients that forms at the surface of the melt pool [2]. The direction of the Marangoni force changes depending on the surface tension gradient, which affects the overall shape of the melt pool [3,4]. Capillary forces form due to the surface tension of the melt pool as well as the curvature of the melt pool [5]. The magnitude of the capillary force can lead to capillary instability, which is responsible for the formation of humps during the printing process [6]. Buoyancy forces are caused by density differences in the liquid metal pool⁵. The buoyancy force effects the direction of flow of material depending on its density⁷. Using the definitions of these forces described in [8] and typical processing parameters for 304L stainless steel described in [9], the magnitude of the forces were approximated for the

exposed portion of the melt pool, which is proportionate to the spot size of the laser. The recoil force is approximated an order of magnitude larger than the Marangoni force, nine orders of magnitude larger than the capillary force and eight orders of magnitude larger than the buoyancy force. With the recoil force magnitude being at least an order of magnitude larger than the next greatest force once it forms, it is the main driving force on the dynamics of the melt pool.

The influence of the recoil pressure can be seen with the different melting modes of the melt pool. If the recoil pressure is too low, heat transfer in the melt pool operates in the conduction mode, leading to poor fusion between the molten material and the previous layer and resulting in brittle parts. Conversely, if the recoil pressure is too high, convection in the melt pool is the dominant heat transfer mode, depressing the melt pool into multiple previous layers and potentially creating keyhole porosity due to the increased absorptivity and making the melt pool less stable [10,11]. This melting mode is referred to as the keyhole mode [12]. Since part quality is primarily driven by these defects, it is important to understand recoil pressure to operate the SLM process between the conduction and keyhole modes, thus, minimizing the potential for these defects.

Important parameters in the SLM process such as melt pool dimensions [3,13], surface height and melt track diameter [14], and keyholes and humps in the scan path [6,15] have been extensively investigated with both experimental and simulation studies. However, relatively little work has conducted to understand recoil pressure as it is very difficult to measure. The recoil pressure has been estimated from the melt pool surface temperature using the Clausius-Clapeyron model. Using this model, the magnitude of the recoil pressure was estimated to be on the order of 86 kPa for a 316L stainless steel

simulation for a laser power of 200 W and scanning speed of 1.5 m/s [16]. Dynamic changes at the melt pool surface have been attributed to changes in the recoil pressure magnitude. The amount of ejecta emitted from the melt pool [17] and spatter formation mechanisms and dynamics [18]–[23] were all hypothesized to change with recoil pressure, whose magnitude determines the amount of vaporization at the melt pool surface. However, the magnitude of the recoil pressure was not quantified in these studies.

The relative velocity of spatter ejected from the melt pool due to recoil pressure can be studied using Particle Image Velocimetry (PIV). Recently, several studies have been able to infer the recoil pressure from the velocity history of particles ejected from the melt pool using in-situ high speed imaging. Zhao et al. estimated an average pressure above the melt pool of 60 kPa for Ti-6Al-4V powder melted with a laser power of 210 W and scanning speed 0.5 m/s in a 2D setup illuminated with synchrotron radiation [24]. This approach requires the assumption that the particles are moving parallel to the imaging plane. Yin et al. calculated a vapor pressure of 49 kPa for Inconel powder processed with a laser power 1150 W and a scanning speed of 1 m/s by observing spatter tracks using high-speed visible camera imaging. Significant complications to these measurements arise with the presence of the gas that flows over the build plate (i.e., shielding gas) to create an inert atmosphere as it substantially modifies particle velocities. Shielding gas was present during the experiment in the Inconel study[25] to prevent melt pool oxidation; however, it was not present in the Ti-6Al-4V study[24].

The PIV studies described above have uncertainties such as assuming the particles move in the same plane as the imaging device as well as the effects of shielding gas on the motion of the particles that affect recoil pressure measurements. To analyze recoil pressure

without these uncertainties, a direct measurement method is desired. For a laser beam diameter of 70 μm , the equivalent force was calculated to be on the order of 0.25 mN using the recoil pressure calculation from the Ti-6Al-4V study [24]. Measuring a force of this magnitude is possible with transducers such as strain gauges; however, it requires specially fabricated, non-commercial equipment. This study will use a commercial accelerometer to measure the vibration of a part that is excited with the laser and quantify recoil force in the frequency domain. Working in the frequency domain allows the frequency content of the recoil force to be isolated from components that are due to the machine running. This measurement technique also contains uncertainties, most notably the magnitude of the Frequency Response Function (FRF) and changes to material properties as a function of temperature. There is a relationship between the FRF and the material properties: the properties dictate the resonant frequencies and the magnitude at resonance. As the part's temperature changes, the FRF inevitably would also change. Uncertainties in the FRF magnitude from user excitation were addressed by taking averages; the uncertainties in the FRF due to changes in the material properties as a function of temperature were addressed by measuring the FRF immediately after the part was pulsed with the laser to reduce the transient thermal effects.

This study proposes a method to measure the recoil force in SLM processes and will investigate the relationships between recoil force and a variety of processing parameters and scanning strategies for SLM of 304L stainless steel. This is achieved by scanning over a tuning fork structure and scaling the magnitude of the force peak at the frequency of the laser to approximate the total input recoil force. The relationship between the recoil force and the laser power, scanning speed, Pulse Repetition Frequencies (PRF),

layer thickness, and path profiles will be analyzed and compared to microstructure data to see whether or not porosity is present for large recoil force measurements as well as lack of fusion for low recoil force measurements.

2. EXPERIMENTAL SET-UP

The experiments conducted in this paper utilize an SLM machine (Renishaw AM250). The SLM machine is equipped with an Acousto-Optic Modulator (AOM) to vary laser pulse duration to create a stable melt pool [26,27], thereby allowing the frequency content of the recoil force to be adjusted in a controlled manner. By adjusting the laser pulse duration, the laser frequency can match the resonant frequency of the tuning fork being processed, thus, ensuring a large Signal to Noise Ratio (SNR) of the accelerometer signal. A schematic of the laser striking a tuning fork, a schematic of the melt pool dynamics during a laser scan, and FRFs (simulated in ANSYS) relating prong acceleration to applied force for tuning forks with various prong lengths are shown in Figure 1.

Figure 1a illustrates the processing of a thin layer of powder on top of a tuning fork prong, which is printed flat (i.e., parallel to the build plate). Part vibration is measured with an accelerometer (PCB 352C34) having a bandwidth of 12 kHz. The tuning forks were printed at 60° relative to horizontal so the laser would excite the bending modes and the parts could be printed without support structures. The melt pool dynamics during the laser scan are shown schematically in Figure 1b.

In Figure 1, the laser beam is heating the powder and droplets (i.e., ejecta) are being vaporized and expelled from the melt pool surface due to the recoil pressure. When the

melt pool surface exceeds the evaporation temperature, i.e., $T > T_{Evap}$, a metallic vapor jet forms and exerts a pressure (i.e., recoil pressure) on the melt pool surface.

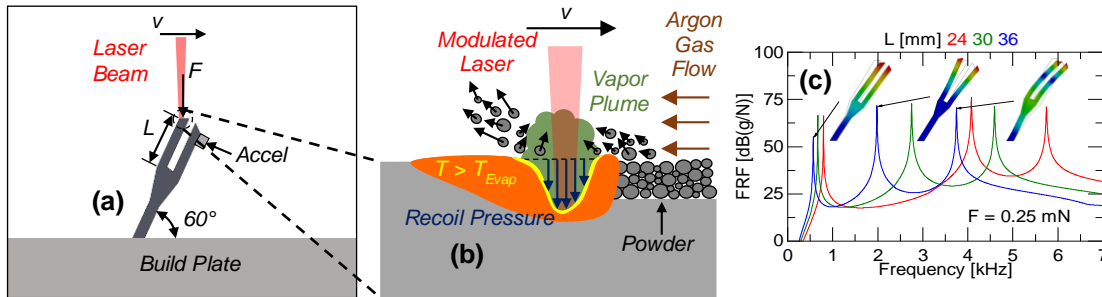


Figure 1: Illustrations of (a) laser excitation of tuning fork with accelerometer (Accel) mounted on tuning fork prong, (b) laser interaction with powder on top of tuning fork during laser excitation, and (c) FRFs of tuning forks with varying prong lengths.

The FRF relating the tuning fork acceleration to the recoil force is

$$FRF(f) = a(f)/F(f) \quad (7)$$

where f is the frequency, a is the part acceleration and F is the force applied to the part. This force consists of all of the forces applied to the melt pool, namely, capillary (i.e., surface tension) force, thermo-capillary (i.e., Marangoni) force, and recoil force [1,28,29] but the magnitude of the force is primarily due to the recoil force; the approximations for each force can be seen in the Methods portion of the paper. Frequency response simulations of three tuning forks having prong lengths of 28, 30, and 32 mm were conducted in ANSYS and are shown in Figure 1c. The tuning fork mode shapes at their respective resonant frequencies are included as insets. By varying the prong lengths, multiple tuning fork

modes can be excited in a range of laser pulse frequencies typically used in SLM processing. From Equation (7), the recoil force frequency spectrum is,

$$F(f) = a(f) / FRF(f) \quad (8)$$

and is determined experimentally using the measured acceleration and the tuning fork FRF computed from tap tests. An SLM build was used to fabricate 40 tuning forks (Figure 2a), 12 of which were used in the experiments conducted in this paper. The build parameters that were used to print the tuning forks were a laser power of 200W, scanning speed of 0.8 m/s, exposure time of 75 μ s, hatch spacing of 85 μ m, and point distance of 60 μ m. The FRF of each tuning fork was measured with a modal impact test by striking each prong vertically with an impact hammer (PCB 086E80) and measuring the corresponding acceleration. The resonant frequencies of each tuning fork used are given in Table 1.

Table 1: List of tuning forks used in experiments with their resonant frequencies.

Tuning Fork #	Resonant Frequency [kHz]	L [mm]
15	10.02	35
16	10.03	36
17	9.930	37
20	9.800	41
27	6.300	49
29	6.300	51
30	6.175	52
31	11.02	53
32	5.200	54
33	5.490	56
34	6.256	57
39	2.050	62

Note that some tuning forks had the same (i.e., #27 and #29) or similar (i.e., #15 and #16) resonant frequencies while having different prong lengths. This is due to the slight deviations from the design drawings due to surface roughness from the SLM process for two parts that are nearly identical. A FRF of tuning fork #16 is shown in Figure 2b. The dominant resonance of the tuning fork in Figure 2b occurs at 10.031 kHz. The resolution of controlling τ_{Pulse} is 10 μs , thus a PRF of 10.0 kHz will be used for experiments conducted on this tuning fork.

The frequency content of the laser, however, is not a pure impulse. Further, the distance between subsequent laser strikes may change when the build direction changes, thus, causing a change in the time between laser strikes. These effects will alter the frequency content of the laser input. To capture these effects, photodiode data was collected during the fabrication of a rectangular part (width 3.85 mm and length 6.35 mm) on a build plate. The photodiode (Thorlabs PDA100A2), having a bandwidth of 11 MHz, recorded laser radiation scattered from an alumina disk target in the middle of the build chamber.

A picture of the photodiode signal, with an inset of the SLM raster scan, and the magnitude of the Fast Fourier Transform (FFT) of the photodiode data are shown in Figure 3. The photodiode signal is characterized by a total pulse period, denoted τ_{Pulse} . The laser duty cycle is $1 - \tau_{\text{Delay}}/\tau_{\text{Pulse}}$. The delay time between pulses is $\tau_{\text{Delay}} = 10 \mu\text{s}$ and is constant; however, the effective delay time, i.e., $\tau_{\text{Delay+Corner}}$ in Figure 3a, can increase or decrease when the laser path changes direction and shifts by the hatch spacing. This motion is often referred to as cornering. The laser/AOM dynamic response is characterized by rise times of 1 μs and 10 μs and a fall time of 10 μs .

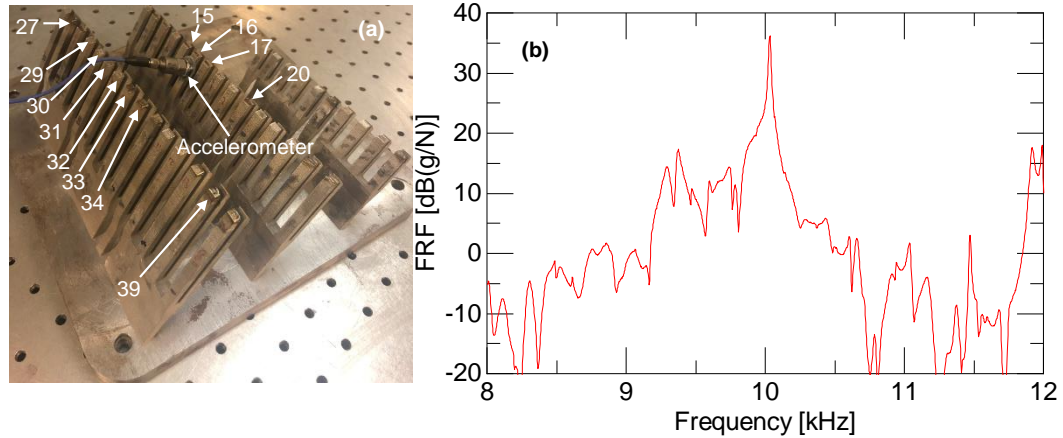


Figure 2: (a) Tuning fork build with arrow indicating tuning forks from Table 1 and (b) FRF of tuning fork #16.

For $\tau_{\text{Pulse}} = 100 \mu\text{s}$, a single line of length 6.2 mm and a raster pattern over an area of $6.35 \times 3.85 \text{ mm}^2$ with 42 straight lines were fabricated and photodiode data was collected. The laser PRF of the single line, given by the red curve in Figure 3b, was concentrated at 10 kHz with harmonics at integer multiples of 10 kHz.

The laser PRF of the raster pattern is given by the blue curve in Figure 3b. The dominant peak shifts from 10 to 9.98 kHz and the magnitude decreases by 0.5%. This energy loss in the dominant peak is conserved through additional frequency content in the form of side bands. Instead of trying to resolve both the harmonics and the sidebands, the only frequency component that is measured for this scan path is the first harmonic (i.e. 9.98 kHz peak seen in Figure 3b).

Once the magnitude of the force at the PRF harmonic is measured, it is scaled to account for the percentage of energy present in the PRF peak relative to the total recoil force.

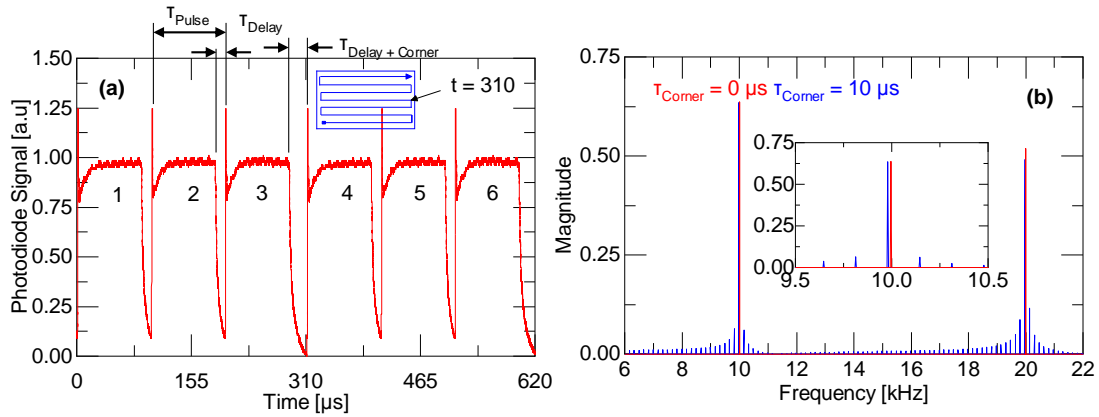


Figure 3: (a) Normalized photodiode waveform with inset showing raster scan and (b) FFT of photodiode waveform data at $\tau_{Pulse} = 100$ μ s with and without cornering.

This is performed considering the magnitude of the recoil force in the time domain will be distributed across multiple harmonics in the frequency domain. This methodology is detailed in the Methods portion of the paper. For every experiment in this study, to prevent aliasing of the PRF peak magnitude, the frequency resolution, df , is selected such that it is a factor of the PRF, i.e., $\text{rem}(PRF/df) = 0$.

3. EXPERIMENTAL RESULTS

3.1. SINGLE LINE SCAN PATH WITHOUT POWDER

A straight-line scanning strategy was used to excite the tops of the tuning forks in this section. For the experiments conducted in this section, the PRF was set to be 10 kHz and the scanning speed was set to be 10 mm/s. No powder was present on top of the specimens. A frequency resolution of 4 Hz was used, which required a sample duration of 250 ms. To obtain this duration, the relationship between the thickness of the prong into

the page in Figure 1a, 6.35 mm, which is constant across all tuning forks, and point distance (PD) between laser strikes, and PRF was derived,

$$T_{Sample} = \frac{6350}{PD \cdot PRF} = \frac{6350}{PD \cdot 10000} = \frac{0.635}{PD} \quad (9)$$

For a PD of 1 μm , T_{Sample} was calculated to be 0.635 s. T_{Sample} needed to be larger than 0.25 seconds in order capture the entirety of the laser pulse, which was longer than 0.25 seconds. To prevent transient errors from the beginning and end of the laser pulse, 0.25 seconds was used that was the middle-most part of the pulse waveform; this ensured that the data was in steady state and did not have the roll-off behaviors seen in the waveforms shown in Figure 3a.

Experimental results for tuning fork #16 are shown in Figure 4. Tuning fork #16 was pulsed with a PRF of 10 kHz, scanning speed of 10 mm/s, and varying laser powers for a total of 9 laser excitations. The experimentally measured FRFs and acceleration spectrums are shown in Figure 4(a,b), respectively. The inset of Figure 4b shows the straight line scanning strategy that was used. The calculated forcing spectrum is shown in Figure 4c, and the grey line in Figure 4c is the SNR, defined as the ratio of the forcing spectrum and the Noise Equivalent Force (NEF), the calculation of which is described in the Methods section.

The peak at 10 kHz in Figure 4a was approximately 18 dB than the next highest peak in the spectrum. The peak at 5.25 kHz is higher in magnitude than the 10 kHz but the SNR at 5.25 kHz is 0.003 while the SNR at 10 kHz is 187. The calculated forcing and SNR spectrums in Figure 4c illustrate that the peak at 10 kHz has an SNR that is approximately

an order of magnitude larger than the SNR of the next highest peak; therefore, most of the energy of the force signal occurs at a frequency of 10 kHz.

The experiment conducted on tuning fork #16 was repeated for tuning forks #15, #17, and #20. Each tuning fork was pulsed with a PRF of 10 kHz, scanning speed of 10 mm/s, and varying laser powers for a total of 9 excitations per tuning fork. The recoil force magnitude for various laser powers for all four tuning forks is shown in Figure 5.

The magnitude of the recoil force scales linearly with laser power as shown in Figure 5. The slope of a fitted regression line was calculated to be 0.12 mN/W. The positive slope indicates that with a higher laser power, there is a higher force. This can be explained through increased vaporization at the melt pool surface. The x-intercept of the regression line was calculated to be 49W, meaning that for laser powers less than 49W, there is not enough energy to melt the powders. The linear relationship between the recoil force and laser power can be explained through a first order approximation model using Rosenthal's solution [30] for a moving point heat source and the Clausius-Clapeyron (CC) model. For changes in laser power, the temperature distribution of the surface increases linearly in the Rosenthal model.

Referencing the CC equation that defines the pressure above the melt pool, shown in Equation 10, where P_o is the pressure at which the material boils, λ is the evaporation energy per particle, K_B is the Boltzmann constant, T_B is the temperature at which the material boils and T is the surface temperature of the melt pool. Given that the temperature operates near the boiling point, the recoil pressure can be seen to behave linearly.

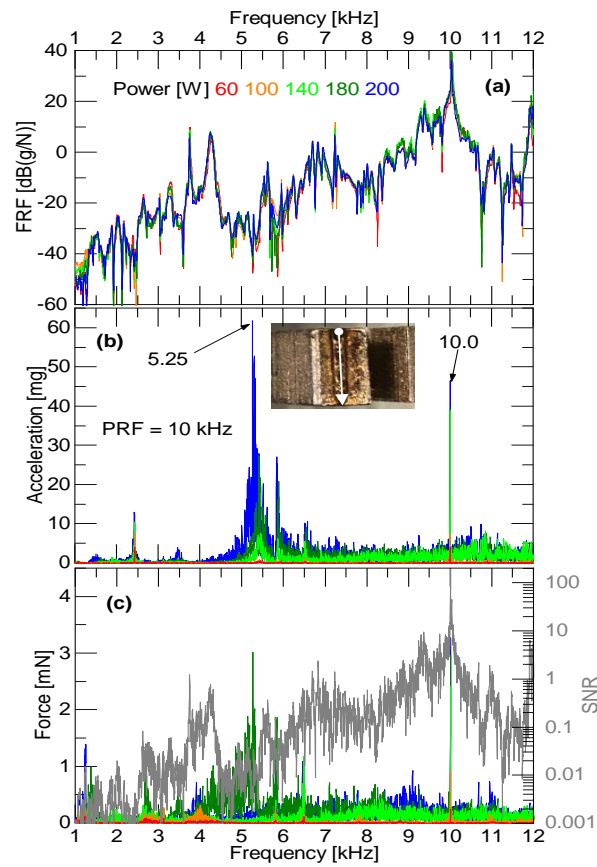


Figure 4: (a) Measured FRFs of tuning fork #16, (b) Measured acceleration spectrum with inset showing single line scanning strategy schematic, and (c) Calculated forcing spectrum with SNR spectrum (gray line).

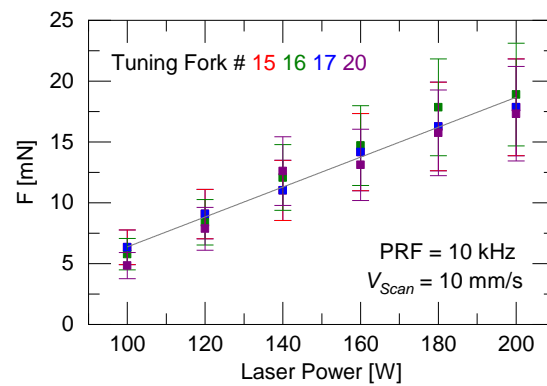


Figure 5: Recoil force versus laser power for tuning forks #15, #16, #17, and #20.

The results from Figure 5 showed consistency of the recoil force across different parts for a constant PRF and scanning speed for variances in the laser power with no powder on the surface for a single line scan.

$$P(T) = 0.54P_o \exp\left(\frac{\lambda}{K_B} \left(\frac{1}{T_B} - \frac{1}{T}\right)\right) \quad (10)$$

3.2. RASTER SCAN PATH WITH LAYER OF POWDER

This section will investigate the effects laser power, powder, and isolated effects of PRF and scanning speed on the recoil force when using raster patterns typical for SLM processes. Further, the tuning forks in this section had a layer of powder of 50 μm , which is typical for SLM of 304L stainless steel [31], spread across the top surface of a prong using feeler gages.

The scanning speed was varied by changing the point distance of the scan path while maintaining the same PRF. To prevent the point distance from affecting τ_{Pulse} , the point distance was kept below 60 μm to prevent changing τ_{Delay} of the laser pulse. The recoil force as a function of laser power and scanning speed, as well as the relationship between the recoil force and the combination of laser power and scanning speed, can be seen in Figure 6.

The magnitude of the forces in Figure 6a were an order of magnitude less than Figure 5a because the scan velocity was an order of magnitude larger. For a constant PRF, the recoil force scaled proportionately with laser power and was inversely related to scanning speed as seen with Figure 6b. Referencing the CC model and the Rosenthal solution for scanning speed, the temperature distribution is inversely proportional to the

exponential of the scanning speed. For different scanning speeds, the recoil pressure behaves approximately linear with scanning speed, which is the same trend that is shown in Figure 6b.

The effects of different PRFs for a constant scanning speed were investigated to see if the recoil force changes depending on the frequency that was used to pulse the melt pool. Tuning forks were excited for PRFs of 5.26, 5.55, 6.25, and 11.1 kHz for a constant scanning speed of 316 mm/s. To maintain a constant scanning speed, the point distance was changed depending on the PRF that was used. The recoil force as a function of laser power for various PRFs is shown in Figure 7a, and the recoil force as a function of the power times the duty cycle, which is the fraction of a single pulse in which the pulse is on, of the different laser pulses is shown in Figure 7b.

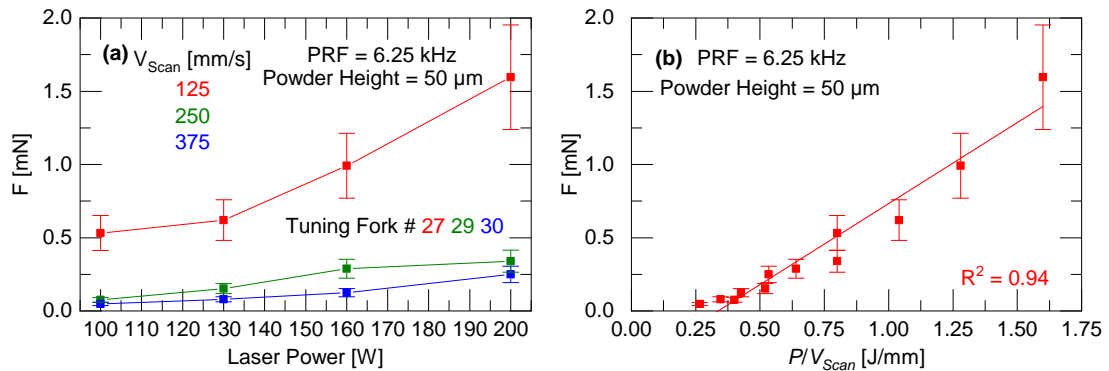


Figure 6: (a) Recoil force as function of laser power and scanning speed for constant PRF and powder layer thickness and (b) Recoil force as function of ratio of power to scanning speed.

The recoil force data in Figure 7a scales linearly with laser power for the different PRFs and scales linearly with the product of the laser power and duty cycle of the pulse in Figure 7b. The slope of the trendline in Figure 7b is positive, meaning that for a higher duty cycle, the magnitude of the recoil force increases.

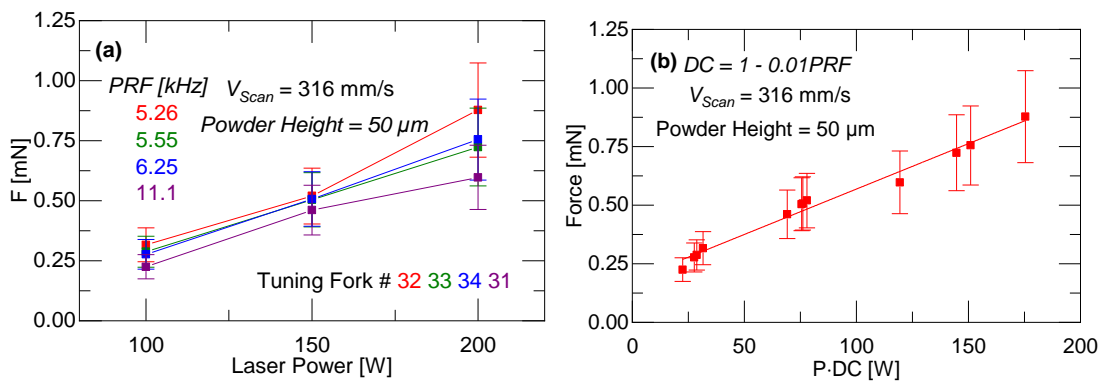


Figure 7: (a) Recoil force as function of laser power and PRF for constant scanning speed and powder layer thickness and (b) Recoil force as function of ratio of power to the square root of PRF.

This agrees with [32] which found changes in the melt pool depth for variances in the PRF of the laser and hypothesized that the recoil pressure was proportional to the duty cycle of the pulse used.

To capture the effects from laser power, scanning speed, and duty cycle, recoil force data was plotted versus $P \cdot DC / V_{Scan}$. The data encompassed both the single line scan data as well as the raster scan data; the recoil force data is shown in Figure 8. The recoil force data scales approximately linear with the ratio of $P \cdot DC / V_{Scan}$. The color scheme that

separates the data in Figure 8 corresponds to the recoil force ranges for transition (green), and keyhole melting modes (blue) with and without powder.

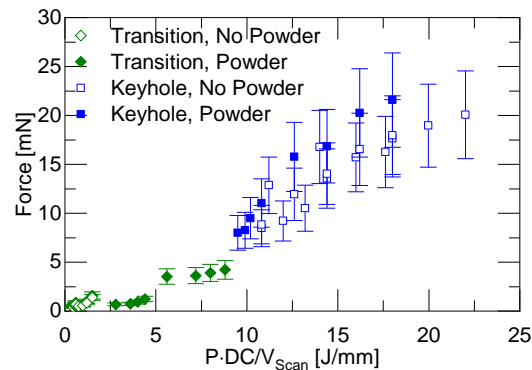


Figure 8: Recoil force as function of $P \cdot DC / V_{Scan}$.

When the energy approaches 10 J/mm, there is a change in the melting mode (transition to keyhole). Having a layer of powder spread on the surface can account for the shift in the force magnitude for similar processing parameters near the transition/keyhole regimes. The keyhole melting mode appears to be more sensitive to changes in the processing parameters than the transition region. The increased sensitivity for the keyhole mode can be explained through increased absorptivity in the melt pool, leading to the recoil force being more sensitive. The variation for the keyhole data is larger than the transition data. This is the case because confidence intervals for the measurements were approximately the same, resulting in the uncertainty being proportionate to the magnitude of the force. The microstructure data that illustrated these ranges is shown in the following section.

The laser powers, scanning speeds, and PRFs that were used in the single line scan were repeated with 50 μm of powder spread on the surface in addition to the raster scan experiments without powder on the surface. Both studies were conducted to investigate the influence of a single layer of powder on the magnitude of the recoil force. The recoil force magnitudes for both no powder and powder are shown in Figure 9.

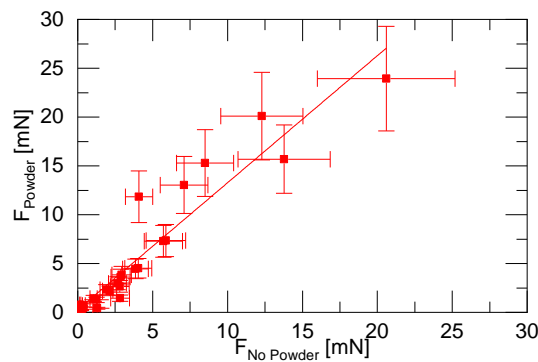


Figure 9: Recoil force magnitude for having powder spread on surface and having no powder on surface for various laser powers, scanning speeds, and PRFs.

The relationship between the recoil force magnitude and powder is approximately linear, shown in Figure 9. The slope of the regression line is 1.3, indicating that the recoil force increases by 30% when a 50 μm layer of powder is spread across the top surface. The absorptivity of the surface increases with powder because of multiple scattering of the laser. Ease of vaporization is also higher with a loose layer of powder since the material is disjointly connected.

3.3. MEASUREMENTS OF MELT POOL AFTER SOLIDIFICATION

To understand the effects of the recoil force on the melt pool, specimens were printed that had the same cross section as the tuning forks that were excited in the previous experiments with a height of 5mm, leading to a volume of $6.35 \times 3.85 \times 5$ mm. The melt pool depth as a function of recoil force for both powder and no powder on the surface is shown in Figure 10a. The influence of powder was studied on the melt pool depth which is shown in Figure 10b. The aspect ratio of the melt pool as a function of the recoil force is shown in Figure 10c; horizontal dashed lines were included that showed the aspect ratios that corresponded to changes in the mode of the melt pool. The range of aspect ratios for the conduction, transition, and keyhole mode are less than or equal to 0.5, greater than 0.5 and less than 1.1, and greater than or equal to 1.1, respectively^{33,34}. Micrographs of sample PRFs and scanning speeds were plotted in Figure 10d to qualitatively show changes in the melt pool with respect to laser power, scanning speed, PRF, and influence of powder on the top surface of the part.

The depth of the melt pool scales linearly with recoil force, seen by the red regression line in Figure 10a. This agrees with current literature given that with an increase in recoil pressure, there is further depression of the melt pool into pre-existing layers [35]. The melt pool depth as a function of powder is seen in Figure 10b.

The micrographs shown in Figure 10d have two groups of 6 micrographs: the first two columns have keyhole melting modes and the last two columns have transition melting modes. Keyhole porosity can be visually seen with the keyhole melting mode micrographs whereas no porosity was seen with the transition mode.

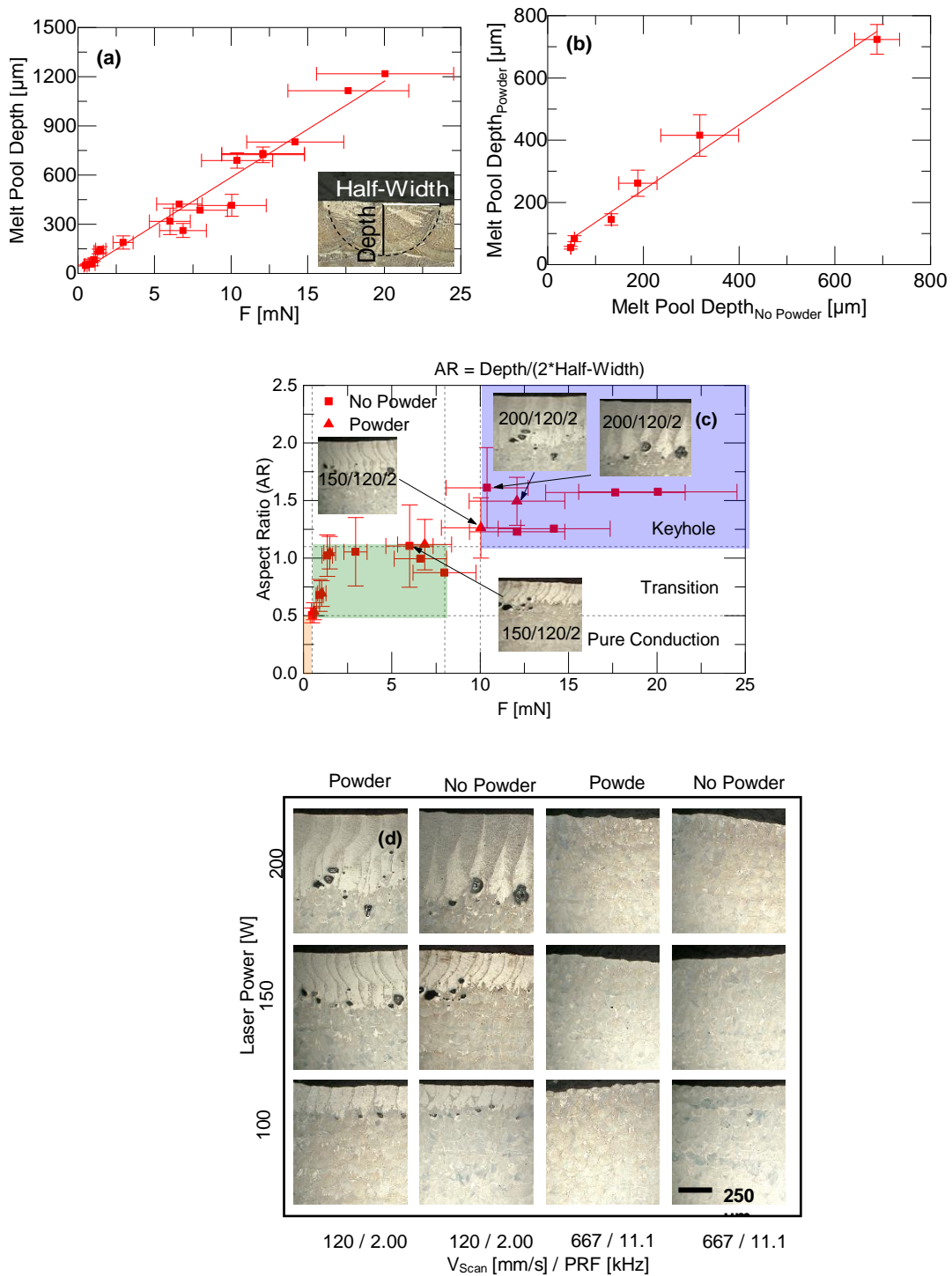


Figure 10: (a) Melt pool depth as function of recoil force with and without powder, (b) Melt pool aspect ratio as function of recoil force with horizontal lines indicating dominant heat transfer modes, (c) Melt pool depth for experiments with powder versus melt pool depth for experiments without powder, and (d) Sample micrographs as function of laser power and scanning speed for raster scan paths with and without powder.

4. METHODS

4.1. MATERIALS

The material used in this study was 304L stainless steel. The chemical composition of the powder can be seen in Table 2.

Table 2: Chemical composition of 304L stainless steel powder.

Element											
C	Cr	Cu	Fe	Mn	N	Ni	O	P	S	Si	
Wt %	0.018	18.4	< 0.1	Bal	1.4	0.06	9.8	0.02	0.012	0.005	0.63

4.2. RECOIL FORCE MAGNITUDE CORRECTION

The bandwidth of the accelerometer used is from 0 to 12 kHz, limiting the ability to resolve higher order harmonics directly. However, the total energy can be inferred from the energy in the first harmonic. This is dependent on the duty cycle of the pulse. Figure 11 shows the fraction of energy in the first harmonic relative to the total energy of the measured photodiode signal. If the force response scales similarly to the photodiode data, this allows the total acceleration (or recoil force) to be estimated by measuring the only the 1st harmonic.

Using the percentage data in Figure 11, the total recoil force was estimated using the following equation, where a is the acceleration of the tuning fork during the laser

excitation, FRF is the experimentally measured FRF of the tuning fork. By using the percentage data, the total input force magnitude can be used to accurately compare PRFs.

$$F = \frac{a(f)}{FRF(f)} \cdot \frac{M_{Input}}{M_{Fund}} \quad (11)$$

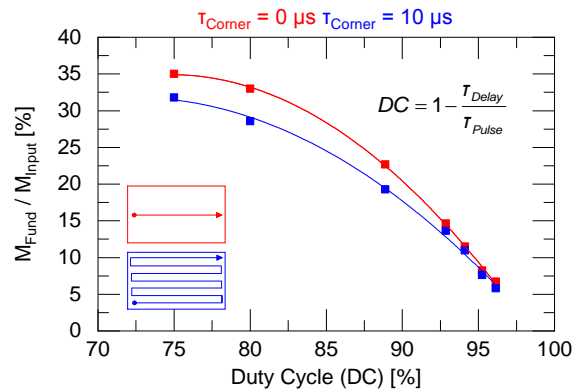


Figure 11: Percentage of energy located in fundamental frequency relative to normalized input for photodiode pulse data pure pulse train and raster scan data.

4.3. UNCERTAINTY CALCULATION

The uncertainty in the force measurements was defined using the following propagation of uncertainty,

$$F_{Unc}(f) = |F| \sqrt{\left(\frac{E_{Accel}(f)}{A(f)}\right)^2 + \left(\frac{E_{Force}(f)}{F(f)}\right)^2} \quad (12)$$

where E_{accel} and E_{Force} are the margins of error for a 95% confidence interval, defined below, for the measured FRFs as well as how the acceleration spectrums were processed.

The margin of error is defined as,

$$E = Z_{\alpha/2} \frac{\sigma}{\sqrt{N}} = 1.96 \frac{\sigma}{\sqrt{N}} \quad (13)$$

where Z is the normal distribution indexed at the confidence level of interest, σ is the standard deviation of the FRFs, and N is the number of FRFs taken.

5. SUMMARY

This experiment quantified an equivalent recoil force induced by the recoil pressure that acts over the melt pool through ex-situ laser excitation of SLM printed tuning forks using a vibration-based approach. The following conclusions can be drawn from the results of this study:

- Recoil force is proportionate with laser power and inversely proportionate with scanning speed and the square root the PRF of a pulsed laser
- Recoil force increases by 30% and melt pool depth increases by 4% by adding 50 μm of powder on surface of part
- Melt pool depth increases linearly with recoil force
- Recoil force values less than 0.5 mN operate in conduction mode, between 0.5 and 8 mN operate in transition mode and greater than 10 mN operate in keyholing mode.

REFERENCES

- [1] Mazumder, J., Ki, H. & Mohanty, P. S. Role of recoil pressure, multiple reflections, and free surface evolution during laser keyhole welding. *ICALEO 2002 - 21st Int. Congr. Appl. Laser Electro-Optics, Congr. Proc.* 33, (2002).
- [2] Chen, Q., Guillemot, G., Gandin, C. A. & Bellet, M. Numerical modelling of the impact of energy distribution and Marangoni surface tension on track shape in selective laser melting of ceramic material. *Addit. Manuf.* 21, 713–723 (2018).
- [3] Wu, Y. C. et al. Numerical modeling of melt-pool behavior in selective laser melting with random powder distribution and experimental validation. *J. Mater. Process. Technol.* 254, 72–78 (2018).
- [4] Zhang, W. Probing Heat Transfer, Fluid Flow and Microstructural Evolution During Fusion Welding of Alloys. PhD Diss. 312 (2004).
- [5] Panwisawas, C. et al. On the role of thermal fluid dynamics into the evolution of porosity during selective laser melting. *Scr. Mater.* 105, 14–17 (2015).
- [6] Tang, C., Le, K. Q. & Wong, C. H. International Journal of Heat and Mass Transfer Physics of humping formation in laser powder bed fusion. 149, (2020).
- [7] Xiao, B. & Zhang, Y. Marangoni and Buoyancy effects on direct metal laser sintering with a moving laser beam. *Numer. Heat Transf. Part A Appl.* 51, 715–733 (2007).
- [8] Heeling, T., Cloots, M. & Wegener, K. Melt pool simulation for the evaluation of process parameters in selective laser melting. *Addit. Manuf.* 14, 116–125 (2017).
- [9] Lough, C. S. et al. Correlation of SWIR imaging with LPBF 304 L stainless steel part properties. *Addit. Manuf.* 35, 101359 (2020).
- [10] Madison, J. D. & Aagesen, L. K. Quantitative characterization of porosity in laser welds of stainless steel. *Scr. Mater.* 67, 783–786 (2012).
- [11] Trapp, J., Rubenchik, A. M., Guss, G. & Matthews, M. J. In situ absorptivity measurements of metallic powders during laser powder-bed fusion additive manufacturing. *Appl. Mater. Today* 9, 341–349 (2017).
- [12] Rai, R., Elmer, J. W., Palmer, T. A. & Debroy, T. Heat transfer and fluid flow during keyhole mode laser welding of tantalum, Ti-6Al-4V, 304L stainless steel and vanadium. *J. Phys. D. Appl. Phys.* 40, 5753–5766 (2007).

- [13] Aggarwal, A., Patel, S. & Kumar, A. Selective Laser Melting of 316L Stainless Steel: Physics of Melting Mode Transition and Its Influence on Microstructural and Mechanical Behavior. *Jom* 71, 1105–1116 (2019).
- [14] Sharma, S., Mandal, V., Ramakrishna, S. A. & Ramkumar, J. Numerical simulation of melt pool oscillations and protuberance in pulsed laser micro melting of SS304 for surface texturing applications. *J. Manuf. Process.* 39, 282–294 (2019).
- [15] Le, K. Q., Tang, C. & Wong, C. H. On the study of keyhole-mode melting in selective laser melting process. *Int. J. Therm. Sci.* 145, (2019).
- [16] Khairallah, S. A., Anderson, A. T., Rubenchik, A. & King, W. E. Laser powder-bed fusion additive manufacturing: Physics of complex melt flow and formation mechanisms of pores, spatter, and denudation zones. *Acta Mater.* 108, 36–45 (2016).
- [17] Zhang, M. J., Chen, G. Y., Zhou, Y., Li, S. C. & Deng, H. Observation of spatter formation mechanisms in high-power fiber laser welding of thick plate. *Appl. Surf. Sci.* 280, 868–875 (2013).
- [18] Taheri Andani, M., Dehghani, R., Karamooz-Ravari, M. R., Mirzaeifar, R. & Ni, J. Spatter formation in selective laser melting process using multi-laser technology. *Mater. Des.* 131, 460–469 (2017).
- [19] Ly, S., Rubenchik, A. M., Khairallah, S. A., Guss, G. & Matthews, M. J. Metal vapor micro-jet controls material redistribution in laser powder bed fusion additive manufacturing. *Sci. Rep.* 7, 1–12 (2017).
- [20] Zhao, C. et al. Real-time monitoring of laser powder bed fusion process using high-speed X-ray imaging and diffraction. *Sci. Rep.* 7, 1–11 (2017).
- [21] Zhang, Y., Fuh, J. Y. H., Ye, D. & Hong, G. S. In-situ monitoring of laser-based PBF via off-axis vision and image processing approaches. *Addit. Manuf.* 25, 263–274 (2019).
- [22] Taheri Andani, M., Dehghani, R., Karamooz-Ravari, M. R., Mirzaeifar, R. & Ni, J. A study on the effect of energy input on spatter particles creation during selective laser melting process. *Addit. Manuf.* 20, 33–43 (2018).
- [23] Guo, Q. et al. Transient dynamics of powder spattering in laser powder bed fusion additive manufacturing process revealed by in-situ high-speed high-energy x-ray imaging. *Acta Mater.* 151, 169–180 (2018).
- [24] Zhao, C. et al. Bulk-Explosion-Induced Metal Spattering during Laser Processing. *Phys. Rev. X* 9, 21052 (2019).

- [25] Yin, J. et al. Correlation between forming quality and spatter dynamics in laser powder bed fusion. *Addit. Manuf.* 31, 100958 (2019).
- [26] Fischer, P. et al. Microstructure of near-infrared pulsed laser sintered titanium samples. *Appl. Phys. A Mater. Sci. Process.* 78, 1219–1227 (2004).
- [27] Fischer, P. et al. Sintering of commercially pure titanium powder with a Nd:YAG laser source. *Acta Mater.* 51, 1651–1662 (2003).
- [28] Qiu, C. et al. On the role of melt flow into the surface structure and porosity development during selective laser melting. *Acta Mater.* 96, 72–79 (2015).
- [29] Shrestha, S., Rauniyar, S. & Chou, K. Thermo-Fluid Modeling of Selective Laser Melting: Single-Track Formation Incorporating Metallic Powder. *J. Mater. Eng. Perform.* 28, 611–619 (2019).
- [30] Promopatum, P., Yao, S. C., Pistorius, P. C. & Rollett, A. D. A Comprehensive Comparison of the Analytical and Numerical Prediction of the Thermal History and Solidification Microstructure of Inconel 718 Products Made by Laser Powder-Bed Fusion. *Engineering* 3, 685–694 (2017).
- [31] Sutton, A. T., Kriewall, C. S., Leu, M. C., Newkirk, J. W. & Brown, B. Characterization of laser spatter and condensate generated during the selective laser melting of 304L stainless steel powder. *Addit. Manuf.* (2020) doi:10.1016/j.addma.2019.100904.
- [32] Caprio, L., Demir, A. G. & Previtali, B. Influence of pulsed and continuous wave emission on melting efficiency in selective laser melting. *J. Mater. Process. Technol.* 266, 429–441 (2019).
- [33] Qi, T. et al. Selective laser melting of Al7050 powder: Melting mode transition and comparison of the characteristics between the keyhole and conduction mode. *Mater. Des.* 135, 257–266 (2017).
- [34] King, W. E. et al. Observation of keyhole-mode laser melting in laser powder-bed fusion additive manufacturing. *J. Mater. Process. Technol.* 214, 2915–2925 (2014).
- [35] Dai, D. & Gu, D. Effect of metal vaporization behavior on keyhole-mode surface morphology of selective laser melted composites using different protective atmospheres. *Appl. Surf. Sci.* 355, 310–319 (2015).

SECTION

2. CONCLUSIONS

In this study a new NDT method was hypothesized to be able to be used on AM parts with the purpose of determining if a part has formed defects during the SLM process. One contribution from this work was showing how modal properties vary depending on the number of parts on a common base plate and while not perfectly resolved at this point, there is a method to correct the coupling effect that occurs when using modal analysis. By adjusting the amount of modal mass in the structure aside from the mass of the part that is being tested, the coupling effect diminishes. A fundamentally novel contribution was defining a novel technique to measure the processing force in AM. This measurement technique can be used for other materials to determine ranges of processing parameters that lead to different melt pool modes that occur during the printing process. Overall, the results from this study can conclude that modal analysis is a promising NDT method. Future work is to finish a comprehensive modal paper that defines a framework to determine sensitivities of part properties and geometries with an acceptance window that can be used to determine whether a part is accepted from its frequency response.

REFERENCES

- [1] D. L. Bourell, J. J. Beaman, and T. Wohlers, “History of Additive Manufacturing,” *Addit. Manuf. Process.*, pp. 1–8, 2020, doi: 10.31399/asm.hb.v24.a0006548.
- [2] B. Berman, “3-D printing: The new industrial revolution,” *Bus. Horiz.*, vol. 55, no. 2, pp. 155–162, 2012, doi: 10.1016/j.bushor.2011.11.003.
- [3] S. V. Murphy and A. Atala, “3D bioprinting of tissues and organs,” *Nat. Biotechnol.*, vol. 32, no. 8, pp. 773–785, 2014, doi: 10.1038/nbt.2958.
- [4] E. Fish, “Rapid Prototyping : How It ’ s Done at GM,” *Automot. Des. Prod.*, pp. 1–4, 2011.
- [5] B. Brown, “Characterization of 304L stainless steel by means of minimum input energy on the selective laser melting platform,” *Mech. Aerosp. Eng.*, p. 100, 2015.
- [6] B. Zhang, Y. Li, and Q. Bai, “Defect Formation Mechanisms in Selective Laser Melting: A Review,” *Chinese J. Mech. Eng. (English Ed.)*, vol. 30, no. 3, pp. 515–527, 2017, doi: 10.1007/s10033-017-0121-5.
- [7] H. Gong, K. Rafi, H. Gu, T. Starr, and B. Stucker, “Analysis of defect generation in Ti-6Al-4V parts made using powder bed fusion additive manufacturing processes,” *Addit. Manuf.*, vol. 1, pp. 87–98, 2014, doi: 10.1016/j.addma.2014.08.002.
- [8] A. Haboudou, P. Peyre, A. B. Vannes, and G. Peix, “Reduction of porosity content generated during Nd: YAG laser welding of A356 and AA5083 aluminium alloys,” *Mater. Sci. Eng. A*, vol. 363, no. 1–2, pp. 40–52, 2003, doi: 10.1016/S0921-5093(03)00637-3.
- [9] L. Thijs, F. Verhaeghe, T. Craeghs, J. Van Humbeeck, and J. P. Kruth, “A study of the microstructural evolution during selective laser melting of Ti-6Al-4V,” *Acta Mater.*, vol. 58, no. 9, pp. 3303–3312, 2010, doi: 10.1016/j.actamat.2010.02.004.
- [10] Q. Y. Lu and C. H. Wong, “Additive manufacturing process monitoring and control by non-destructive testing techniques: challenges and in-process monitoring,” *Virtual Phys. Prototyp.*, vol. 13, no. 2, pp. 39–48, 2018, doi: 10.1080/17452759.2017.1351201.

- [11] V. M. Keppens, J. D. Maynard, and A. Migliori, “Listening to Materials: From Auto Safety to Reducing the Nuclear Arsenal,” *Acoust. Today*, vol. 6, no. 2, p. 6, 2010, doi: 10.1121/1.3467645.
- [12] B. M. West *et al.*, “Modal analysis of metal additive manufactured parts,” *Manuf. Lett.*, vol. 13, pp. 30–33, 2017, doi: 10.1016/j.mfglet.2017.06.001.

VITA

Tristan Cullom was born in Fort Brag, North Carolina on July 13th, 1996. He graduated from Warrenton High School in 2014. From high school, Tristan pursued a Bachelor of Science degree in Mechanical Engineering at Missouri University of Science and Technology and graduated Summa Cum Laude in May of 2018. After graduation, Tristan started graduate school in a Master's degree program in Mechanical Engineering at Missouri University of Science and Technology in the summer of 2018. Tristan completed his Master's program August of 2020, under the guidance and direction of Dr. Robert Landers, Dr. Douglas Bristow, and Dr. Edward Kinzel.